January 2021

Photometric And Astrometric Analysis Of Three Near-Earth Asteroids

Steven D. Newcomb

PHOTOMETRIC AND ASTROMETRIC ANALYSIS OF THREE NEAR-EARTH ASTEROIDS

by

Steven Duane Newcomb
Bachelor of Arts, California State University Sacramento, 2004

A Thesis
Submitted to the Graduate Faculty

of the

University of North Dakota

In partial fulfillment of the requirements

for the degree of

Master of Science

Grand Forks, North Dakota

May
2021

Name: Steven D. Newcomb

Degree: Master of Science

This document, submitted in partial fulfillment of the requirements for the degree from the University of North Dakota, has been read by the Faculty Advisory Committee under whom the work has been done and is hereby approved.

DocuSigned by:
Sherry Fieber-Beyer
Dr. Sherry Fieber-Beyer

DocuSigned by:
Mike Gaffey
Dr. Mike Gaffey

DocuSigned by:
Wayne Barkhouse
Dr. Wayne Barkhouse

This document is being submitted by the appointed advisory committee as having met all the requirements of the School of Graduate Studies at the University of North Dakota and is hereby approved.

DocuSigned by:
Chris Nelson
Chris Nelson
Dean of the School of Graduate Studies

3/3/2021
Date

PERMISSION

Title Photometric and Astrometric Analysis of Three Near-Earth Asteroids

Department Space Studies

Degree Master of Science

In presenting this thesis in partial fulfillment of the requirements for a graduate degree from the University of North Dakota, I agree that the library of this University shall make it freely available for inspection. I further agree that permission for extensive copying for scholarly purposes may be granted by the professor who supervised my thesis work or, in her absence, by the Chairperson of the department or the dean of the School of Graduate Studies. It is understood that any copying or publication or other use of this thesis or part thereof for financial gain shall not be allowed without my written permission. It is also understood that due recognition shall be given to me and to the University of North Dakota in any scholarly use which may be made of any material in my thesis.

Steven D. Newcomb
May 2021

ACKNOWLEDGEMENTS

The author offers appreciation to those who provided their time, effort, knowledge, and expertise to help in the thesis process:

- Sean McCloat
- Cedric Ramesh
- Devi Dina
- Bev Fetter
- Brian D. Warner

The author also extends gratitude to the members of the thesis advisory committee, Dr. Michael J. Gaffey, and Dr. Wayne A. Barkhouse. Thank you for your time and support in this endeavor.

In addition, deep thanks and appreciation goes to Dr. Sherry Fieber-Beyer, for serving as advisor and committee chair, and for providing feedback, guidance, advice, and support throughout this process.

TABLE OF CONTENTS

LIST OF TABLES

LIST OF FIGURES

ABSTRACT

Asteroid astrometry can provide precise information on an object's orbital position and motion, while lightcurve photometry can help determine its rotational spin rate, its shape, and the possible presence of a binary satellite object in orbit around it.

This thesis therefore reports the astrometric and photometric study of three near-Earth objects (NEOs): 68347 (2001 KB67), 494999 (2010 JU39), and 455432 (2003 RP8). Because NEOs represent a record of the early solar system, serve as possible sources for minable material, and sometimes present an impact hazard to the planet Earth, the study of these asteroids is important for understanding their orbital nature and movement through the environment of space.

Data were collected remotely using the University of North Dakota Space Studies Observatory in Emerado, North Dakota. I controlled the observation through an internet interface, and on-the-ground telescope operators assisted with both the software and hardware.

All images were calibrated using AstroImageJ software. Data analysis was carried out in MPO Canopus. The results indicate that 68347 (2001 KB67) had a Total Rate of Motion (TRM) of approximately 518.855 ± 141.000 ”/hr. Using a third harmonic order, the derived period is 6.350 ± 0.045 hrs. Its diameter is approximated at 324 ± 61.225 m.

494999 (2010 JU39)'s TRM was approximately 1651.147 ± 100.897 "/hr. Using a third harmonic order, its period is 2.828 ± 0.024 hrs. Further, its diameter is estimated to be 355 ± 67.132 m.

The TRM for 455432 (2003 RP8) was calculated at 665.331 ± 81.244 "/hr. Period analysis showed a rotational rate of 4.200 ± 0.01 hrs. Its size was estimated to be approximately 708 ± 13.395 m.

The period analysis for 68347 (2001 KB67) and 455432 (2003 RP8) complimented the findings of previously published research. However, the spin rate calculated for 494999 (2010 JU39) fell far below the prior published estimate, by approximately 27.9 hrs.

CHAPTER 1

INTRODUCTION

Although there are competing ideas about its exact mechanisms (e.g. Morbidelli et al., 2009; Weidenschilling 2010), the generally accepted theory of the planetary building process proposes that large bodies known as planetesimals accreted from smaller particles that were present within the early nebula, and that these planetesimals then went on to form the core of the planets in our solar system (Safronov, 1972). Asteroids are the leftover remains of this planet-building.

Asteroids are studied for a multitude of reasons. Understanding the processes that guided and influenced their formation, for example, can give clues into the events of the early solar system, such as the occurrence of solar T. Tauri heating (Sonett et al., 1968; Menzel & Roberge, 2013). Further, studying their ongoing evolution can also provide insight into current dynamics, such as space weathering (e.g. Willman & Jedicke, 2011).

Asteroids that come within the orbit of the Earth, known as near-Earth objects (NEOs), potentially pose an ongoing threat to the safety of the planet. For example, in the early 1980's, geologic evidence (Alvarez et al., 1980) was found that linked a possible asteroid impact with the mass extinction that occurred during the end of the Cretaceous period 66 million years ago. A decade later, the 180 diameter Chicxulub crater, located partially off the coast of the Yucatan Peninsula, in Mexico, was identified as the probable strike location for the impactor (Hildebrand et al, 1991). Although this type of strike itself is an extreme and relatively rare occurrence, as recently as 2013 (Borovicka et al., 2013), a bolide (a meteor that explodes within the Earth's atmosphere) occurred over Chelyabinsk, Russia. The object began to fragment at an altitude between 45 and 30 km, before completely crumbling as it got closer to the surface. Its explosion

gave off energy that was roughly equal to about 500 kilotons of TNT and caused damage to buildings on the ground. Because of the continuing danger such events pose, Reinhardt et al. (2016), performed a probabilistic risk assessment on the possibility of a catastrophic asteroid strike, finding the probability of such an occurrence to be 0.0007%.

In addition, asteroids also hold potential monetary value for countries and companies that can successfully develop and launch the technology needed to conduct mining missions. Fieber-Beyer and Gaffey (2019), for example, examined the composition of 162385(2000 BM19), an asteroid that had been previously designated as a target for possible mining interests. They found that its minerology was composed of pyroxene and olivine and was most closely matched to the composition of LL chondrite meteorites. Although LL Chondrites do not typically contain a lot of metal, what little they do have consists of many, if not all, of the platinum-group metals, and these could hold tremendous market value if mined in mass quantiles from a large body.

Because asteroids can tell us a tremendous amount about our own solar system, and about the threats and opportunities it holds, my thesis research focuses on the photometric and astrometric study of three NEOs, the asteroids 68347 (2001 KB67), 494999 (2010 JU39), and 455432 (2003 RP8).

Overview of Near-Earth Objects

Asteroid Taxonomy

To better understand the types of asteroids that comprise the near-Earth population, it is important to understand the overall concept of asteroid taxonomy. Taxonomic types vary based on the classification being applied, and numerous systems have been advanced over time.

The most widely used system, developed by Tholen (1984), was originally derived from photometric observations taken from the *Eight-Color Asteroid Survey (ECAS)*, and radiometric

data taken from the *Thermal Radiometric Survey*. The analysis looked at five hundred and eighty-nine asteroids. The visual data was narrowed through the use of principal components analysis that reduced the information from the survey's seven color indices into two components (the indices u-v and v-x). Cluster analysis was then performed on the photometric and radiometric data to derive seven major asteroid classes (A, C, D, E, M, P, S), three minor classes (B, F, G), a possible eighth major class (T), and three asteroids that did not fit into any of the existing categories and were therefore labeled as R, Q, and V.

The current version of the Tholen system is made up of 14 classes (A, B, C, D, E, F, G, M, P, Q, R, S, T, V), each based on distinctive spectral features of the asteroid. For instance, asteroids falling under the D category are distinguished by low albedo and a red spectrum with no distinguishing features, while those under the T category have low albedo and a red slope leading up to .75 μm (Cellino et al., 2002, p. 637).

An alternative taxonomy was developed by Bus & Binzel (2002), using data collected from the *Small Main-belt Asteroid Spectroscopic Survey (SMASSII).* Based on CCD Spectroscopy of 1447 asteroids, Bus & Binzel (2002) originally intended to categorize each object by utilizing the Tholen system. However, to classify a new asteroid, Tholen relied on comparisons with the data taken from ECAS. Because the SMASSII utilized a spectral wavelength range, between 0.44 and 0.92 μm, that was only partially covered in ECAS, it was not possible to properly categorize the new objects with the old system. Due to this incompatibility, Bus & Binzel (2002) pursued an alternative taxonomy. The new system, which consists of 26 unique spectral asteroid types (A, B, C, Cb, Cg, Cgh, Ch, D, K, L, Ld, O, Q, R, S, Sn, Sk, Sl, Sq, Sr, T, V, X, Xc, Xe, and Xk), includes many of the Tholen groups, but also added classifications that better fit portions of the new data.

Another taxonomy, developed by DeMeo et al. (2009), and known as a Bus-DeMeo system, was based on near-infrared (between 0.45 to 2.45 μm) spectral data of 371 asteroids. It is a revision of the SMASSII system described above, except that it includes 24 spectral types. It eliminates Ld, Sl, and Sk, and creates a new category, Sv, to serve as a bridge between S and V type asteroids.

Although taxonomies often overlap each other in terms of asteroid classification, they are not without their limitations. For instance, Gaffey et al. (1993) pointed out that for generalized classes, such as S, A, and M, the asteroids represented within often include subtypes that vary from one another in terms of mineral composition and thermal modification. These asteroids, therefore, should not be treated as a lump category, but instead should be investigated, either individually or as part of their sub-types, for their unique properties.

Further, as Binzel et al. (2015, pp 246) indicated, "the taxonomic classification produced by these measurements is only a first step toward understanding an object's composition…any compositional suggestion from taxonomy is an interpretation, not a certainty; taxonomy is not a substitute for detailed mineralogical analysis."

Although additional debate on the limitations of asteroid classifications goes beyond the scope of this present thesis, taxonomy is still important to note, as it is applied to the study of NEOs when determining their physical properties. For example, Lin et al. (2018) used definitions from the Bus-DeMeo system to help classify 92 NEOs collected during photometric observations. From these efforts, objects were divided into seven spectral classifications (A, C, D, Q, S, V, and X). Most of the objects were shown to be S and Q types. These classifications, in combination with known albedo measurements, allowed for size estimation of many of the asteroids.

Orbital Classifications of NEOs

Based on the individual parameters of their orbits, NEOs are divided into one of three main orbital groups: Aten, Apollo, and Amor asteroids. More specifically: Aten asteroids have a semimajor axis (a) < 1 AU and intersect Earth's orbit at an aphelia (Q) > 0.983 AU; Apollo asteroids have a > 1.0 AU, and a perihelion distance (q) < 1.017 AU; Amor asteroids have a q that falls between 1.017 and 1.3 AU, with orbits that do not intersect that of the Earth's (Shoemaker, Et. al, 1979).

Potentially Hazardous Asteroids (PHAs)

Marsden (1997) proposed a subset category for Potentially Hazardous Asteroids (PHAs), He defined these objects as having an absolute magnitude of H < 20, having a diameter that is ≥ 1 km, and having a Minimal Orbital Insertion Distance (MOID) of ≤ 0.05 AU. More recently, the Center for Near Earth Object Studies (CNEOS), has used H ≤ 22 as a limit in defining these types of objects (Chodas, 2020).

Amount and Size Distribution of NEOs

The estimated number of NEOs, and the range of their sizes, has been studied. Harris and D'Abramo (2015), for instance, performed a computer simulation that sampled observations made between 2012 and 2014. They then calculated how many of the observations were of new objects, and how many were for objects that had been previously recorded. Additionally, because not all NEOs have an equal chance of being observed at a given sample time, an estimation of the probability of unequal discoveries of new objects vs. known objects was factored in. From this analysis, the number of near-Earth Objects ≥ to 1 km in diameter was determined to be around 990.

Similarly, Tricarico (2016) looked at 10,033 nights of near-Earth asteroid data that were taken by nine different surveys conducted over several decades. Combining these observations into a single analysis, he focused only on asteroids with maximum velocities that did not exceed 100 arc-seconds-per-hour. He also compensated for trailing loss. This was defined as the amount of light not received, or "lost," for a single pixel in a CCD array, due to the continuous movement of the asteroid. From this, he found that the estimate for large NEOs with diameters of 1 km or larger was lower than expected, at 920 ± 10. For the smaller diameter population, less than 1 km, the estimate was $(4 \pm 1)\ x10^8$.

Origins and Composition of NEOs

The population of near-Earth asteroids is comprised of objects representing the full spectrum of taxonomic types (Binzel et al., 2004; Binzel et al., 2019). However, the bulk of the population appears to be composed of S and Q types (Binzel et al., 2004). Because ordinary chondrites (OCs) make up a large percentage of the meteorite samples recovered on Earth, it is logical to conclude that they derive from the most common asteroid types. However, early attempts at linking asteroid types to the meteorite samples collected here on Earth did not bear much evidence for this idea. Chapman & Salisbury (1973), for example, compared the reflective spectra of 41 sampled meteorites, including 22 OCs, to the spectra of 38 main belt asteroids. It was found that the two types of samples did not pair well, with few of the meteorites matching with the asteroids. The authors made note that two of the asteroid types, R3A and R3B, now classified in modern taxonomy as S-type objects, had spectra that were similar to that of the OC samples, with an absorption feature around 1μm. However, the spectra of the asteroids were not as curved as those of the OC meteorites, and it had a slope that was more linear into the region of infrared.

Feierberg et al. (1981) examined the spectra, between 0.09-2.5 μm, of 11 S-type asteroids to compare their composition with that of both differentiated and non-differentiated meteorite types. They found that the asteroids had a minerology that matched closet to that of both carbonaceous and ordinary chondrites but did not match well with meteorites that were differentiated. However, later studies (e.g. Gaffey,1984) that attempted to directly link spectra of OC meteorites to that of S-class asteroids found that the S-type objects had a spectral slope that was redder than that of OC samples, and were not a comparable match.

To explore possible causes of the mismatch between meteorite and S-type asteroids, Bell & Kell (1987) looked at whether the effects of space weathering could alter OC material to the point where its spectra would match that of an S-type. More specifically, Bell & Kell (1987) obtained meteorite samples that were compromised both of material that had been exposed for an extended duration to space, and of material that had not been exposed to such conditions, and then measured the spectra of both. From this, Bell & Kell (1987) did not observe evidence of S-type spectra in the space-weathered regions of the samples. They then concluded that space weathering was probably not altering S-type surfaces in a way that would explain their spectra.

However, several years later, evidence to the contrary began to surface, starting when the initial data from the Galileo spacecraft flyby of S- type asteroid 951 Gaspra (Belton et al., 1992) showed variation in color and albedo among some of the object's surface features. The brighter areas were thought to have been material that had undergone some sort of movement through weathering, and therefore was "fresher." These areas also showed a stronger absorption feature at 1 μm than did the darker, non-weathered areas, providing evidence that weathering could indeed alter spectra.

To study the overall composition of near-Earth asteroids, Binzel et al. (1996) collected the spectra of 35 objects between the range of 0.45 and 0.95 μm. They found that the majority of the S asteroids in the sample displayed a moderate absorption band close to 1 μm. This indicated the presence of olivine and pyroxene. However, six of the sampled objects had profound absorption bands near 1 μm. The spectra for these six objects were closest to that of asteroid 1862 Apollo, which itself had previously been identified as a mixture of pyroxene, olivine, and metal, and was similar in composition to that of ordinary chondrite (OC) meteorites. There are significant differences between the band depths for H, L, and LL chondrites, and for the six sampled asteroids, it was theorized that they matched closest to the H6 subclass. However, because of the limitations on the spectra, no solid conclusion could be made. For the additional 29 asteroids in the sample, the distribution of their spectra showed a continuum between S and Q types, making it difficult to distinguish Q-type objects from S-type objects. Binzel et al. (1996) proposed several possible explanations for this continuum. First, the asteroids may have been fragments of a larger, mineralogically diverse body and thus represented the range of compositions for a single object. Conversely, variety in the size of the particles comprising the regolith of each object could also result in the band depth ranges that were measured. Finally, because many near-Earth asteroids are small (often under 3 km in diameter), they may undergo random collisions more frequently, and be resurfaced more often than larger objects. When sampling from an unrelated group of smaller objects, all of which experienced collisions at different times, a variety of surface ages may be apparent. The variety of surface composition, then, would contribute to the continuum in the spectra that were measured.

Veverka et al. (2000) reported on the results of the Near- Earth Asteroid Rendezvous (NEAR) mission that launched in 1997 to further investigate the surface properties and

composition of S-type asteroids. It was inserted into orbit around 433 Eros on February 14, 2000. The spacecraft contained instruments such as the Multispectral Imager (MSI) and the NEAR Infrared Spectrometer (NIS). Data from both instruments were collected over a two month period, from February 14, 2000, to April 1, 2000. The craft was held in an orbit 200 km from the target object. Spectra taken of the asteroid showed an absorption feature around 1000 μm that represented olivine and pyroxene, and another absorption feature around 2000 μm that represented pyroxene. According to Veverka et al. (2000), thousands of reflectance spectra were also taken using the NIS, covering wavelengths from 800 to 2300 μm. When averaged together, the spectrum showed features consistent with other S-type asteroids. More specifically, it had an overall composition that contained olivine, orthopyroxene, and possibly some type of iron, and was similar to the mineralogy of OCs, and in particular matched closest to either an L or a LL chondrite.

Vernazza et al. (2008) measured the spectra of 38 S and Q asteroids. The data were collected using the SpeX spectrograph at the NASA Infrared Telescope Facility (IRTF) in Hawaii and were combined with visual wavelength observations of the same asteroids that were taken from previous studies. This was then compared to laboratory spectra for a sample of 57 OC meteorites. Vernazza et al. (2008) used a technique, known as the radiative transfer model, that allowed for an estimation of the ratio between olivine and orthopyroxene. For OCs, this ratio was estimated to be an average of 63%. For the observed S and Q asteroids, with space weathering effects accounted for, the ratio was around 69.6%. From this, Vernazza et al. (2008) concluded that near-Earth objects tend to contain more olivine than do most OC meteorites, but they are comparable matches for LL chondrites, which have olivine/orthopyroxene ratios that fall between 70 and 85%. However, the fact that LL chondrites only account for a small portion of

OCs suggested that they may come from larger bodies that undergo natural processes, such as the YORP effect (discussed below), in a much slower manner than smaller rocky objects, such as the bodies thought to be responsible for the delivery of most meteorites to Earth. Because the orbits of larger objects would only change over very long periods, they would most likely originate from a region that is close to a natural resonance. Expanding on this, Vernazza et al. (2008) suggested that, in the main belt, the S-type objects in the Flora asteroid family sit close to the ν_6 resonance, and they have an olivine/orthopyroxene ratio similar to that of LL chondrites, suggesting that they may be a major source contributing to the NEO population.

Nakamura et al (2011) analyzed grain particles that had been collected by the Hayabusa spacecraft during its mission to S-class near-Earth asteroid 25143 Itokawa. The sample was removed from its collector in two ways: The first group of grains were extracted by a spatula instrument, and the second were collected when the sampler was tapped and the particles allowed to fall onto a glass slide. For the spatula group, the sample consisted of 1534 grains that were sized between 3 to 40 μm. The composition was a mix of minerals, including 580 particles that were olivine, 126 that were low-Ca pyroxenes, 56 that were high-Ca Pyroxenes, 113 that were troilites, and 447 that were mostly silicates. For the glass slide group, the grains were between 10 and 50 μm. The grains were composed of various minerals, including olivine and low and high-Ca pyroxene. Nakamura et al (2011)'s analysis revealed that 32 of the glass slide particles were strongly equilibrated, and six were weakly equilibrated. For the highly equilibrated particles, it meant that they had undergone extensive metamorphism through the process of thermal heating. They were similar in composition to the particles found in LL5 and LL6 chondrite meteorites. In contrast, the weakly equilibrated particles were closer in composition to LL4 chondrites. This led to the conclusion that Itokawa is composed of breccia

material that represents a mixture of both weakly and strongly equilibrated material. The more metamorphized material was heated deep within the original, larger parent body, and then removed through one or more impact events. The pieces then formed into loose gravel and were bound together by gravity into the current rubble-pile structure of the asteroid (Nakamura et al 2011).

Dunn et al. (2013) collected the spectra of 40 asteroids, between the wavelengths of 0.4 and 1.1 μm, using NASA's SpeX instrument, the small-main-belt asteroid survey (SMASS), and the Palomar Observatory. In addition, they incorporated the spectra of 32 other objects, including V, Q, and S-type asteroids, which had been taken from previous research. This brought the total sample examined to 72, Dunn et al. (2013) then calculated the Band I center for each of the objects and applied newly derived formulas to determine the objects' individual minerology. They found that 47 of the sampled asteroids were comprised of either chondritic material, or material that was similar to that of the ordinary chondrites. Calculations were then done for the abundance of minerals for each asteroid. From this, it was confirmed that the objects matched the composition of ordinary chondrites. The majority, 60%, of this subsample were shown to be LL chondrites. The rest of the group consisted of minerology that was similar to either H or L chondrites, or that represented a mixture that could not be differentiated between L and LL. The diameter was then estimated for all 72 objects. From this, the asteroids were divided into a group for objects that were less than 1km, and into a group for objects that ranged from 1 to 10 km. The two asteroids that were determined to be above 10 km in diameter were excluded from the analysis. The percentage of the H, L, LL, and L-LL borderline asteroids was then calculated for the two diameter groups. The distribution was similar across the two groups. This was a possible indication that smaller bodies do not provide a larger proportion of these meteorites than do

larger objects. Dunn et al. (2013) then utilized a dynamical probability model, originally developed by Bottke et al. (2002), to determine that the asteroids comprised of LL chondrite material more than likely came into the inner solar system through the ν_6 resonance

Origin of Near-Earth Asteroids

Binzel et al. (2004) analyzed near-infrared spectroscopic observations obtained from the Small Main-Belt Asteroid Spectroscopic Survey (SMASS) of 401 near-Earth and Mars-crossing asteroids. The objects were classified using the Bus taxonomic system. Binzel et al. (2004) found that the asteroids in the sample represented the same range of taxonomic types as objects within the main belt, with 25 of 26 classes being observed. Roughly 90% of the observed asteroids fell into the S, Q, X and C classifications, with 40% of NEOs as classified as S-types, and 25% classified as Q-types. Further, Binzel et al. (2004) paired the dynamical modeling technique of Bottke et al. (2002) with their current data to investigate the possible origin source for many of the observed objects. From this, it was found that the ν_6 resonance was the most probable source region for 46% of the observed asteroids, but Binzel et al. (2004) noted that the size of this contribution may have been exaggerated in the sample due to asteroids from this region being easier to discover and observe than those from other sources. Additionally, Mars-crossing orbits contributed 27% of the sampled objects, while the 3:1 resonance contributed 19% and the outer belt contributed 6%. Specifically, the 3:1 resonance and the outer belt were identified as the main source region for C-type asteroids. D-and X type objects were attributed to Jupiter family comets. V-type objects were rarely found in Mars crossing orbits, suggesting that they migrated quickly into the inner solar system, most likely from the ν_6 and 3:1 resonances. S and Q types appear to be related, and evidence suggests that they may originate from the same region. The delivery route for the E-types may have been through the ν_6 resonance, and they may have

originated from the Hungaria region. The C, D, and X subsample had the most members with Tisserand (T) parameters at <3. For the X objects, Binzel et al. (2004) lacked albedo information. They assumed that the X-types with a T < 3 were actually P-types, because they all appeared to originate from the outer belt. It is thought that asteroids with both a T≤ 3 and a low albedo may have cometary origin.

Thomas and Binzel (2010) compared spectra of asteroids collected from the databases of both the Reflectance Experiment Laboratory (RELAB), and the SpeX instrument at NASA's Infrared Telescope Facility (IRTF), to spectra measured from laboratory samples of OC meteorites. The range for both asteroids and meteorites were limited from 0.4 to 2.5μm. 74 sample meteorites were used. This consisted of 19 H, 27 L, 12 LL, and 16 HED. 54 near-Earth asteroids were observed, and the objects represented the S, Sq, Q, and V-type classes. Thomas and Binzel (2010) then mathematically paired the spectrum from each sampled asteroid to that of the sampled meteorite that it was most related to. These asteroid-meteorite pairs were then correlated to the probabilities of individual source regions in an attempt to determine the most likely origin point from where each meteorite type entered the inner solar system. The results indicated that, for all four types, the ν_6 resonance was the likely delivery conduit for most of the samples. However, the H ordinary chondrites were also strongly linked to the 3:1 resonance.

Adding to these discoveries, Granvik & Brown (2018) used computational computer algorithms to trace the orbits of 25 meteorite falls, pulling the data on trajectories, classifications, and ages from previously published work. The reconstructed orbits matched closely to the majority of those displayed by NEOs. Tracing back the history of each orbit showed that most of the objects associated with meteorite falls came from either the inner-main belt, or from the Hungaria group.

Binzel et al (2019), collected spectra, between the wavelengths of 0.8 to 2.5 μm, of 1040 objects. They utilized the SpeX spectrograph at the NASA Infrared Telescope Facility in Hawaii, and the Baade Telescope at Chile's Magellan Observatory, as well as previously or soon-to-be published data that was collected from their colleagues. Mirroring many of the findings discussed above, Binzel et al (2019) again saw all main-belt taxonomic types represented within the sampled near-Earth population. Going further, they applied orbital modeling to each object in the dataset to investigate the potential sources of their origins. From this, it was determined that NEOs of C-type originated from all over the outer main-belt. D-types, on the other hand, were strongly associated with the 2:1 resonance, and with regions where Jupiter-Family Comets (comets with periods of 20 years or less) are found. P-types, which are well represented in the outer main belt, were matched to the 5:2 resonance. L- and Q-types were shown to come from the ν_6 resonance, while V-types, which are linked to the asteroid Vesta as a parent body, were delivered through the 3:1 resonance. Asteroids thought to be linked to specific meteor mineralogy were also studied: H Chondrite objects were tied to the 3:1 and 5:2 resonances; L Chondrite objects were likely delivered through the ν_6 and 3:1 resonances, and also from the Hungaria zone; and LL-chondrite objects likely originated through the ν_6 resonance.

Fieber-Beyer et al. (2015) looked at a possible compositional link between the PHA 2007 LE, and the black, shocked H-chondrite known as Rose City. Spectra for the asteroid was collected in the near-infrared range using the NASA IRTF. The results revealed an absorption feature at 1 μm that was indicative of a mafic minerology. No additional absorption features were observed. Utilizing the asteroid's derived mineral composition, Fieber-Beyer et al. (2015) then compared it to spectra of sampled meteorites. They found that it matched closely to a black OC, Rose City, that displayed a similar 1 μm absorption feature. It was noted that 2007 LE

contained a slightly larger amount of olivine than did the meteorite. This was attributed to the possibility that the Rose City sample had undergone more intense shock than the asteroid itself, and that this shock disrupted the crystal structure of its olivine, making its overall minerology more difficult to accurately measure. The calculated albedos of both the asteroid (0.08) and the meteorite (0.065) were similar enough to suggest a relation. Further, the asteroid's estimated diameter of .5 km lent evidence to the idea that it had been a piece of a larger object, and that it had been separated during a possible collision event. Fieber-Beyer et al. (2015) theorized that both 2007 LE and Rose City could have originated from the suspected H chondrite parent body (6) Hebe. If these objects had fragmented from (6) Hebe, they would have most likely passed through the nearby 3:1 resonance before reaching near-Earth orbit.

As mentioned briefly above, comets have also been considered as a likely source for some NEOs. Osip et al. (1995), for example, studied 4015 Wilson-Harrington, an asteroid that at initial discovery had a coma and tail, but is now considered as being in the transition state from comet to asteroid. Its orbit also crosses that of the Earth's. Performing CCD photometric observations, Osip et al. (1995) produced a lightcurve showing a rotation period of 6.1± 0.05 hrs. and an amplitude 0.2. This matched closely to rotation parameters shown by many other NEOs.

In their study using SMASS data, described above, Binzel et. al (2004) found that, in a sample of 401 near-Earth and Mars-crossing asteroids, the C, D, and X subsample were most likely attributable to cometary origin.

DeMeo & Binzel (2007) searched for near-Earth objects suspected of being cometary in origin. To identify candidate NEOs, they relied on spectral data, albedo information, and on the Tisserand parameter that measures the interaction between a large mass body, such as a planet, and a smaller mass body, such as an asteroid. In this case, the Tisserand parameter for Jupiter

(T_j) was used, with values of T_j <3 being considered as an indication of possible candidates. 20 NEOs were identified, with 4 of them confirmed later as being limited-activity comets. In addition, previously published NEOs were also examined, and 55 were identified with relevant T_j values. Using these findings, DeMeo & Binzel (2007) estimated that 16 ± 5 % of NEOs fit the spectra, albedo, and Tisserand parameters to be described as possible comet nuclei.

Asteroid Rotation

The rotation of asteroids has been a topic of research for many decades. Harris & Burns (1979), for example, performed a statistical analysis of the rotational data taken from a sample of 182 previously published asteroids. They found that the rotation of an asteroid seemed to be determined largely through previous collisions with other objects, and that as an asteroid's size decreased, the rate of its rotation increased. However, Harris & Burns (1979) also found that this varied based on taxonomic type, with C and S-type asteroids showing little change in rotation rate due to size. Specifically, C-types had much slower rotation rates than other asteroids in the sample. This, they concluded, indicated that C-types are comprised of weaker material than what is found in other taxonomic types.

Over a decade later Harris (1996), analyzed rotational trends for a database of 688 asteroids. In particular, he focused on objects that were smaller than 10 km in diameter. He proposed that for the physical structure of an asteroid to stay together, a relationship must exist between its rotational rate and its internal density. In other words, the faster an object rotated, the denser it would have to be, or otherwise it would simply fly apart. For the sample, Harris (1996) found no objects that exceeded the spin limit corresponding to a 2.7 gm/cm^3 density. This, he suggested, was an indication that the asteroids in his sampling could not spin faster, because they were composed of loose "rubble pile" material with lower density and internal cohesion.

In a later study, Pravec and Harris (2000) looked at a sample of 750 asteroids, with 748 being larger than 200 m (0.2 km), and 2 being smaller. For those that were above 40 km in diameter, it was found that their rotation rate was "normal," or about 2.5 revolutions per day. Objects below 40 km showed diversity, with a mixture of both fast and slow rotation. A sizable portion, however, increased in spin as they got smaller, and many were measured as being spherical in shape. There also appeared to be a bottom limit, at 2.2 hrs, for how fast these asteroids could spin. Because of this, and because of their spheroid structure, it was concluded that these asteroids sat near or above the break-up point for rubble pile objects and were probably composed of loosely connected fragments of material held together through gravity. This contrasted to the two asteroids, 1995 HM and 1998 KY26, both NEOs, that had diameters below 200 m. 1995 HM had a period of 1.6 hours, and 1998 KY26 had a rotation rate of only 10.7 minutes. Their small size and rapid rate of rotation suggested that their structure was composed of monolithic material.

Pravec et al. (2002), refined their previous research by looking at an updated database of 984 asteroids. They found that when the asteroids' rotational periods were plotted against their diameters, objects that were roughly above 35-40 km formed an approximate Maxwellian distribution. This suggested that spin for asteroids of this size was the result of collision dynamics between bodies within the main belt. In contrast, objects below the 35-40 km limit had a non-Maxwellian distribution and were varied in their rotational rates. Between 0.15-10 km, the population was a mixture of both slow and rapid rotators. In this range, the 2.2 hr. (11 to 12 rotations per day) limit was again observed, reinforcing the suggestion that many of these asteroids are gravitationally bound rubble piles. But for objects smaller than 0.15 km, the rotation rates were extremely rapid, suggesting a more coherent interior structure. Pravec et al.

(2002) emphasized, however, that this does not necessarily mean that these bodies are comprised of completely solid material. Instead, a diversity of structural configuration can exist, but it must be stronger than that of loosely bound gravel.

Pravec et al. (2002) discovered an exception to the 2.2 hour breakup limit for 2001 OE84. The object, an Amor asteroid, was calculated as having a diameter of 0.7 km, and a rotational rate of 29.191 ± 0.000 minutes. It was one of the first of its kind to be both monolithic, and relatively large, which led Pravec et al. (2002) to conclude that it may have been a large slice from a parent body that was severed during a collision.

Since the discovery of 2001 OE84, however, other large objects with similar rapid rotation have also been observed. Chang et al (2014) reported their photometric observations on main belt asteroid (335433) 2005 UW163 with a diameter of around 0.6 km, and a rotational period of 1.290 hrs. Similarly, Rozitis et al. (2014) observed NEO (29075) 1950 DA and found that it had a diameter of 1.3 km, and a rotational period of 2.122 hours.

Polishook et al. (2016) observed (60716) 2000 GD65, an inner-main belt object with an approximate diameter of 2.3 km. They measured its rotational period as being around 1.953 hours. To explore this finding, Polishook et al. (2016) considered five different models for the asteroid's structure and movement. This included the object being composed of loose gravel bound together through either gravitational or strong cohesion forces, the object being a single monolithic body, the object undergoing a shed of mass, and the object undergoing rotational changes due to the YORP effect From this modeling, cohesion of material was determined as the best fitting explanation.

Chang et al. (2016) used a series of observations taken through the Intermediate Palomar Transient Factory Survey to search for large asteroids rotating faster than the 2.2 hour limit

would dictate. From their efforts, they identified (40511) 1999 RE88, a main-belt object with an approximate diameter of 1.9 km, and an observed rotational rate of about 1.96 hours. In addition, they also detected 18 additional possible candidates that required further study. In explaining these findings, Chang et al. (2016) reported that for an object the size of 40511 to rotate rapidly without breaking apart, it requires the internal materials to have a cohesive strength of around 780 Pa.

Much of this discussion of asteroid rotation has centered on main belt samples, with only a few NEO targets mixed in. However, the rotation rate of the near-Earth population has also been studied. Hergenrother & Whitely (2011), for instance, made direct photometric observations of 62 NEOs. The absolute magnitude (H) of the objects ranged from 20.4 to 27.4. The rotational periods of 8 of the objects could not be determined with any level of reliability. For the rest of the sample it was found that 78% of the objects had a rate of rapid rotation.

Medeiros et al. (2018) used data from the Asteroid Lightcurve Database to conduct a statistical analysis of the spin rates of 13,546 asteroids in the Main Belt and 1,082 in near-Earth orbit. It was found that for larger objects in the main belt (between 50 and 125 km in diameter), much of their current spin appears to be from collisional interactions, and that it can be attributed to torque transfer occurring bi-dimensionally. In contrast, the spin of small main belt objects, as well as NEOs, was ascribed not only to collision, but also to the momentum caused by the absorption, reflection, and re-emission of the Sun's radiation (the YORP effect, described in detail below).

The Yarkovsky and YORP Effects

In his paper detailing the probabilities of planetary collisions, Opik (1951) reintroduced a concept that had been originally postulated decades earlier by civil engineer Ivan Yarkovsky. He

explained this effect as being "produced by the uneven emission of radiation by a rotating body in which a phase lag of surface temperature occurs…When rotation and orbital motion are in the same direction, the Yarkovsky effect produces a positive drag opposite to the Robertson effect and may counterbalance it; when the sense of rotation is opposite to orbital motion, both effects add working in the same direction (Opik, 1951, p. 194)."

Over time, the Yarkovsky effect can alter the orbit of an asteroid. For example, Chesley et al. (2003), used radar data from the Arecibo observatory in Puerto Rico to show that the Yarkovsky effect affected the orbital path of 6489 Golevka.

Building on the idea of the Yarkovsky effect, Vladimir V. Radzievskii (1952) postulated that thrust created by photons could have an affect an object's rotation rate. This was expanded on when Stephen J. Paddack (1969), and John O'Keefe (1976) separately theorized that re-emitted radiation, and not just photon thrust alone, could influence the rotation of a small, irregular-shaped body. This concept was eventually labeled as the Yarkovsky O'Keefe Radzievskii Paddack (YORP) effect by Rubincam (2000). In modern research, both the Yarkovsky and YORP effects have been invoked to fill gaps in our understanding of the nature of NEOs. Bottke et al. (2006), for example, pointed out that the traditional models used to explain how asteroids are pushed from the main belt and into near-Earth orbits, which regularly rely heavily on the idea of collisional disruptions and high velocity ejections, often do not meld well with observation. However, factoring in the orbital effects of thermal re-radiation helps to reconcile the shortcomings of these models, and adds to our understanding of the evolution of NEOs.

The influence of thermal re-emission has also been demonstrated through observational research. For example, in separate studies, Taylor et al. (2007) and Lowry et al. (2007), found

evidence for the YORP effect in the increasing spin rate of the near-Earth asteroid (54509) 2000 PH5. Similarly, Durech et al. (2018) detected acceleration by the YORP effect in asteroids (161989) Cacus and (3103) Eger.

Binary Asteroids

A binary asteroid is an object comprised of a main body that has a secondary natural satellite in orbit around it. Walsh et al. (2008) tested the idea that binary objects can form when gravitationally bound rubble pile object increases rotation through the YORP effect. Through mathematical simulation, they found that because the structure of these objects is only semi-cohesive, "spun-up" material can be expelled from the equatorial region of the main object and form into a tight, circular orbit around the remaining main body.

Cuk (2007) suggested that after the formation of a binary asteroid, the satellite object, once fully accreted, undergoes a binary YORP effect (BYORP). This allows the secondary object to migrate in its orbit. For larger binary objects, such as those seen in NEO populations, this migration can separate the primary and satellite object by a wide distance. If this separation grows large enough, further disruption of the binary pair can occur when combined with gravitational interactions with the Earth or other planets. Smaller objects, however, can tolerate a large separation without experiencing similar disruptions.

Binary asteroids in the near-Earth population are often the focus of study. Pravec et al. (2006), for instance, made photometric observations of 17 binary NEOs. As part of their analysis they calculated for each binary pair the ratio between the diameter of the satellite object and the diameter of the primary body. They found that binaries with a ratio ≥ 0.18 were common for small NEOs (2 km in diameter or less), and that binary configuration was less likely to occur in

larger objects. Further, satellite bodies are apparently limited in size to a diameter ≤ 1 km, and primary objects have fast rotation and a spheroid structure.

Historical Review of Astrometry & Photometry

The current study uses astrometry and photometry to study NEOs. Astrometry is the measure of an object's position and motion, and photometry is the study of the amount of energy, in the form of light, produced by an object. Both have deep historical roots that go back thousands of years.

In 126 BC, for example, Greek astronomer Hipparchus recorded a catalog of over 800 stars. For each object, he marked both its position, as well as how brightly it appeared in the night sky. The scale he used to measure object flux was relatively simple, consisting of three points: Of brilliant light; of second degree; and faint (Hipparchus, 126 BC/1884)

Almost three hundred years later, in 150 AD, Claudius Ptolemy, in his classic text *the Almagest*, catalogued the brightness and position of 1022 stars. Working with a ringed instrument known as an astrolabe, he made observations by applying a scale for measuring object brightness that was made up of six numerical points, with each point being described as a "magnitude." In this system, the brightest stars were rated as being first magnitude, while the dimmest were measured at sixth magnitude. In addition, he provided notes on stars that did not quite fit the magnitude being described, but instead were a bit brighter or fainter than a whole number would allow (Ptolemy, 150 A.D./1984).

Much of the work in the centuries that followed continued to focus on the stars catalogued by Ptolemy. In 964 A.D., for example, Persian astronomer Abd al-Rahman al-Sufi published the *Book of Fixed Stars* ((al-Sufi, ca. 964 A.D./2018). This work used the same star list provided in *The Almagest*. However, the position of each object was re-

calculated to account for precession, and Al-Sufi provided his own magnitude determinations. In this regard, his scale followed the same basic parameters as Ptolemy's (1 to 6) but gave more distinction for objects that fell between whole magnitudes. In his system, stars could be measured at 1, 1-2, 2-1, 2, etc., allowing for more precision.

With the invention and increasing use of the telescope during the 17th century, it was soon realized that a 6-point magnitude scale was insufficient for describing all stellar objects, since many more stars appeared under telescopic magnification than could be observed with the naked eye. Italian astronomer Galileo Galilei was one of the first researchers to demonstrate this, and he found through observation that objects under magnification were at least 5 magnitudes brighter than when viewed unaided (Galilei, 1610/1989).

Around this same period in history, astrometry was also undergoing drastic change. Starting in 1543, with the publication of Nicholas Copernicus's *De Revolutionibus Orbium Coelestium* (Copernicus, 1543/1995), a revolution in the understanding of the motions of heavenly bodies was underway. Copernicus himself had put forth the idea, based on the ancient theories of Greek mathematician and astronomer Aristarchus, that the Earth, along with the other planets, was in orbit around the Sun. This concept was known as heliocentrism.

Once the notion of heliocentricity took root in popular thought, other astronomers began to incorporate it into their own work. One of the most notable examples, Johannes Kepler, sought to describe the nature of the planets' orbits around the Sun. In particular, he attempted to reconcile his observations of Mars with a proper model for orbital motion. He concluded that a circular path was insufficient to explain his data. Instead, he settled on the idea that the planets orbited in an elliptical geometry, and that the Sun served as one of the two foci. This, in turn, became the first of Kepler's laws of planetary motion (Kepler, 1609/1992).

By late 18th and early 19th centuries, photometry continued to evolve. In the late 1700's, for example, astronomer William Herschel noted that some stars, such as a few found in the constellation of Leo, changed their luminosity over time (these are now known as variable stars). Realizing that the typical systems of magnitude previously used in observations were inconsistent in describing these types of stars, he created notation that compared the brightness of a variable to that of a fixed comparison star. (Herschel, 1796, p.530).

Despite the progress being made, by the mid 1800's it had become apparent that discrepancies existed in the way that magnitude was being assigned. Astronomer William Rutter Dawes (1851), for instance, noted that brightness estimations of a single star could vary wildly across multiple observers, and that often astronomers tended to measure stars as being dimmer than they really were. A few years later, N.R. Pogson (1857), an astronomer working from the Radcliffe Observatory in Oxford, England, proposed a solution to the issues raised by Dawe's when he published a table of magnitudes for 36 asteroids. As part of this, he included columns predicting the magnitudes of the objects during each of the twelve months of the year. To derive these values, he used a formula that included a standardized brightness ratio, which measured how much brighter an object is in comparison to another object that is one magnitude fainter, of 2.512.

The use of Pogson's ratio was soon adopted into the research of others, including into the photometric studies being conducted at the Harvard Observatory in Cambridge, Massachusetts, under the tenure of Edward C. Pickering. Pogson's ratio appeared in calculations in the observatory's various catalogues (e.g. Pickering et al, 1884), and was part of an effort to apply a consistent scale of magnitude for an observed comparison.

During the years under Pickering, additional innovations in photometry, including new instrumentation, were also introduced. His Meridian Photometer, for example, was designed to work with a telescope and could be used to observe objects near the Meridian that were brighter than the 10th magnitude. Inside it included two adjustable mirrors. One mirror would be positioned to reflect light from the comparison star, α Ursae Minoris (Polaris), while the other could be directed at the targeted object. The light reflected off the mirrors would travel through a 4 inch aperture lens that had a focal length of 60 inches (two lenses were used, one for each mirror), and then pass through a reversible double-image prism to correct for partial polarization. Light from both mirrors would then be received through an eyepiece that was coupled with a Nicol prism. The image from the Polaris mirror would be compared to that received from the mirror reflecting the observed star. Then the double-image prism was reversed, and the process was conducted again (Pickering, 1882).

In total, the Harvard Observatory collected and worked with a tremendous amount of data. By 1908, for instance, it had observed and catalogued 9110 stars at 6.5 magnitude or brighter (Pickering, 1908a), and 36.682 stars that were dimmer than 6.5 magnitude (Pickering 1908b).

Modern Photometry

Photometry has undergone drastic evolution within the last 150 years. Much of this was spurred by the discovery of the photoelectric effect. This was first described by Heinrich Hertz (1887) when he observed voltage changes in the spark between a pair of metallic electrodes while they were exposed to ultraviolet light. Soon after, Wilhelm Hallwachs (1888) placed a plate made from zinc into a vacuum chamber, exposed it to UV light, and measured the resulting charge that occurred.

In his seminal study on the subject, Albert Einstein (1905) used mathematics to describe how this effect works. He concluded that when a quanta of light (photon) impacts an electron, it can transfer its energy into the atomic particle. The level of energy that is transferred depends only on the frequency of the photon, not on the intensity of the light If this exchange energizes the electron enough, it can escape from its atom and create the measurable charge seen in the photoelectric effect.

Beginning in the early 20th century, these experimental and theoretical findings started to be applied for practical purposes within photometric astronomy. Schulz (1913), for example, experimented with the use of a photoelectric photocell that combined platinum wiring with potassium to measure light from the stars Capella and Arcturus. Similarly, Stebbins (1916) used a photocell consisting of rubidium to observe the light curve from the β Lyrae star system.

By the 1930's, technology once again advanced. While working for the Radio Corporation of America (RCA), Zworykin et al. (1936), introduced the world to photomultipliers. These were devices that used metallic surface material, composed of elements such as Na or Ni, to produce an initial emission, from the photoelectric effect, of electrons. This preliminary stream of particles would then be redirected to bombard another metallic surface and create a secondary particle emission, which, in combination with the first stream, would then be directed to a third surface, and so on, creating a cascading effect. Once this process had been repeated the desired number times, the building stream of particles would be redirected into a collector.

Photomultipliers proved to be a powerful tool for astronomical photometry, with astronomers quickly adapting the technology for the purposes of observation. Kron and Gordon (1947), for example, used a photomultiplier tube, in combination with the Lick Observatory's

12-inch refractor telescope, to obtain the light curves for variable stars RR Lyrae, Tu Cassiopeiae, and T Monocerotis.

By the early 1970's, Boyle and Smith (1970), proposed the use of Charge Coupled Devices (CCD) that utilized semi-conductor material (chips) to store information as electric charges. Photons would displace electrons within the chip, via the photoelectric effect, and the resulting electrical charges could then be shifted into a register and read out as images or as digital video. By the mid 1970's, this technology had started to be adapted into astronomy, and was being used as an efficient way to collect data, such as images of the recently discovered rings around Uranus (Smith, 1977). By the mid 1980's, a CCD camera was being utilized to take images of Halley's comet (Schild, 1985), and by the end of the decade such cameras were being deployed for the purposes of photometry (e.g. Stetson et al., 1989)

Photometry of Asteroids

The current literature review has already touched on multiple examples of asteroid research based on photometric observation. However, Lupishko et al. (2007) noted that, in general, asteroid photometry is regularly used to derive both the spin and overall shape of objects, examine the characteristics of asteroid surfaces, and identify and measure binary pairs.

Speaking from a more theoretical perspective, Li et al (2015), defined modern asteroid photometry as serving multiple purposes. First, measuring light reflected off an asteroid can provide clues to the physical construction of its surface, including how rough, smooth, or porous its material is. Additionally, photometric observations and modeling can provide the geometric corrections that are needed for measurements of an object's reflectance spectra. Further, photometry can also provide information useful for the planning of both instrumental and spacecraft observations.

Modern Astrometry

In the last 120 years, astrometry, like photometry, has also undergone many changes. By the start of the 20th century, improvements in equipment allowed for millions of stars to be imaged simultaneously and measured on a single photo plate. Because so many positions were being recorded, scientists were able to use the data to explore the astronomy of larger scale. In 1905, for example, Jacobus Kapteyn, a Dutch astronomer, reported on "star streaming," where stars could be divided into two distinct groups whose motion were opposite of one another in the sky, hinting at the possibility of larger galactic structural movement (Kapteyn, 1905).

As the 20th century progressed, the use of photo plates fell away as new, more advanced technology was introduced, and by the mid 1970's, as with photometry, the CCD began to be used. In modern astrometric research sky surveys, such as the second US Naval Observatory CCD Astrograph Catalog (UCAC2) (Zacharias et al., 2004) and the Sloan Digital Sky Survey (Gunn et al., 2006) have utilized CCD technology to capture an enormous amount of data, including star positions.

Astrometry of Asteroids

Asteroid astrometry can be used to establish an object's location (measured in declination and right ascension) and movement (velocity measured in arc seconds per hour) in the sky, and to determine its overall orbital characteristics as defined by the six Keplerian orbital elements (Kepler, 1602/1992), eccentricity (*e*), semi-major axis (*a*), inclination (*i*), longitude of the ascending node (Ω), argument of periapsis (ω), and true anomaly (ν). For an orbit to be properly established, long-term observation must follow after initial discovery. Desmars et al. (2013) found that uncertainty in ephemeris, the position of an object over the course of time, decreases as the observation of its orbital arc, the time between first and last observation, increases. To that

point, after reviewing the initial discovery data for a sample of over 10.000 asteroids, Galache et al. (2015) suggested that, to achieve sufficient coverage of an orbital arc, an object should be observed for a period of three or more months.

In investigating the precision of ground based observations, Eggl et al. (2013), found that astrometry with high accuracy, such as that done through radar, accounted for only 2% of observations in 2013 and that most astrometric measurements, conducted through ground based telescopes, are accurate between 0.13" and 2".

To provide high precision astrometric measurements using a space-based instrument, the European Space Agency (ESA) launched the Gaia spacecraft in 2013. The mission's main objective was to accurately determine the positions of 100 billion stars to create a three-dimensional map of the Milky Way (ESA, 2019). As part of this, Gaia was also expected to measure many main-belt and near-Earth asteroids for both relative and absolute positioning (Bancelin et al., 2012).

Five years after Gaia's launch, Spoto et al. (2018) reported on observations made by the spacecraft of a subsample of 14,099 asteroids. It was found that, depending on the brightness of the asteroid, the accuracy of the measurements was below a miliarcsecond. However, multiple factors, such as movement, impaired the preciseness of the results. For asteroids below a magnitude of 16, however, object size also appeared to be the largest contributor of inaccuracies.

Purpose of Current Study

As illustrated above, the study of near-Earth objects is both diverse and extensive. Because these objects serve as a record of the early solar system, as a resource for minable materials, and as a potential impact hazard, it is important to understand their origin, their composition, their orbits and motion, and their interaction with the elements of the space

environment. To this end, the present research focused on the study of three near-Earth asteroids. Astrometric analysis was used to determine each objects' position and movement, and differential photometry was utilized to obtain a light curve and rotational period for each object.

CHAPTER 2

METHODS

Target Asteroid Selection

A running list of NEOs on close approach with the Earth is maintained online by the Jet Propulsion Laboratory (JPL) and the California Institute of Technology (CIT) (Chodas, 2019). The website produces a customizable table that can be adjusted to display items by approach date, nominal distance, and Absolute Magnitude (H). For this study, objects were chosen by upcoming approach dates and by nominal distance.

The target list generated from the website was downloaded into an Excel file. Each asteroid was checked against information provided in the HORIZONS web-interface (Park, 2019). This is another website maintained by JPL and CIT. It provides a customizable search feature that allows the user to choose the object they are targeting, the location of observation, the time span, and other variables. The resulting output shows the date and time the object will appear in the sky of a given location, the air mass, and the object's apparent magnitude. In addition, the output table also displays orbital and rotational information.

Any object with an already-published rotational period was screened out of the selection process. In addition, potential targets also had to be visible from the observing location (discussed below), have an acceptable air mass (< 2, but ideally < 1.5), and be of an apparent magnitude ≤ 16.

The Asteroid Lightcurve Database (LCDB) (Warner, 2011a) was utilized to crosscheck all chosen objects. Any target with a published light curve that included a rotational period was removed from consideration.

Target Objects

Three near-Earth targets were chosen and observed for this study, two of which are defined as Potentially Hazardous Asteroids (PHA). Their designations, orbital information and absolute magnitude are reported in Table 1.

Table 1: Orbital and Absolute Magnitude (H) Information for Targeted Near Earth Asteroids

Object	e	a (AU)	q (AU)	Q (AU)	Period (Yr.)	Orbital Class	H
68347 (2001 KB67)	0.38	0.96	0.60	1.33	0.94	Aten (PHA)	19.9
494999 (2010 JU39)	0.55	0.92	0.42	1.42	0.88	Aten (PHA)	19.7
455432 (2003 RP8)	0.37	1.73	1.10	2.37	2.28	Amor	18.2

Source: (JPL, 2019)

Previously Published Research for the Targeted Objects

At the time of observation, none of the listed objects had a published rotational period, and none had appeared significantly in research literature. However, since data collection, information has been published on all three target asteroids.

For 68347 (2001 KB67) Warner (2018) found its rotational period to be 6.354 ± 0.004, with an estimated diameter of 325 m. No uncertainty for the diameter was provided. Similarly, Loera-Gonzalez et al. (2019) found the period to be 6.357 ± 0.004h with a 0.31 amplitude.

Warner & Stephens (2019) reported a period for 494999 (2010 JU39) of 30.2 hours, based off of a half-period of 15.11 ± 0.04 hours. The published light curve, however, was

incomplete. In addition, the object's diameter was estimated to be 360 m, with no uncertainty provided.

The period for 455432 (2003 RP8) was estimated by Warner & Stephens (2020) at 4.2736 ± 0.001 hours, with an amplitude of 0.55. They noted the lightcurve's asymmetry, suggesting that it could have been the result of shadows that occurred at an increased phase angle. The diameter of the object was estimated at 680 m, with no additional uncertainty provided.

Observation Site & Equipment

All data were collected remotely using the University of North Dakota Space Studies Observatory. The facility is in Emerado, North Dakota, about 14 miles from the main campus of the University. For all nights of observation, I accessed the facilities via a remote connection that logged in through the ACP Observatory Control software. This program package was developed by the company DC-3 Dreams and provided via license. This interface allowed for a pre-scripted observation plan, saved as a text file, to be uploaded and used to give direction to the telescope and camera. At the same time, an on-site telescope operator (TO), or operators, oversaw the hardware, control software, and other elements.

For each asteroid, data collection took place over a series of nights, as the object came into view in the North Dakota sky. All three targets were observed using Telescope #3, which hosted a Meade LX200R telescope with a 16-inch aperture. It was combined with an Apogee U9000 CCD camera. The camera was controlled through the MaximDL software program, which was developed and licensed by Diffraction Limited. The telescope mount control and pointing were accomplished through TheSkyX, software developed and licensed by Software Bisque. And the focuser was controlled through FocusMax, a program designed and licensed by

CCDware. All three of these programs interfaced with ACP and were accessible only to the onsite TOs.

Images for all three asteroids were taken through the R filter. To enhance the signal-to-noise ratio for each object, a 3x3 binning on the CCD was utilized. Exposure times varied per object and are reported in Table 2.

Table 2: Observing Parameters

Object	Apparent Magnitude (m)	Date/Time	Sky Conditions	Img. Exp.	Total # of Images	# of Dark Frames	Dark Exp.	# of Flat Frames	Flat Exp.
68347 (2001 KB67)	15.3	6/3/2018 3:08-6:10 UT	Increasing cloudiness during observation	120s	74	10/night	120s	20/night	1s
	15.5	6/4/2018 3:16-8:50 UT	Mostly clear						
	15.9	6/6/2018 6:19-8:54 UT	Clear						
494999 (2010 JU39)	16.1	6/25/2019 4:40-8:22 UT	Clear	100s	100	10/night	100s	30/night	4s
	15.9	6/26/2019 3:40-7:40 UT	Clear						
455432 (2003 RP8)	14.6	7/29/2019 4:18-8:07 UT	Clear	60s	195	10/night	60s	31/night	2s
	14.8	7/30/2019 3:00-7:49 UT	Increasing cloudiness during observation						
	15.3	8/2/2019 3:1-7:30 UT	A few clouds						

Air Mass and Atmospheric Distortion

Air mass provides a measurement of how far an object's photons travel through the planet's atmosphere. When an object is at an angle, for example, its light must traverse through more molecules than when the same object is at the zenith directly overhead (Warner, 2016. pp. 68). The longer the path of travel, the more likely the incoming photons will be subject to atmospheric effects.

For the current study, all observations across all nights were done when the asteroids were between an airmass of 1 and 2. The timing for this was determined through information found on the JPL Horizons website.

Data Calibration Images

Before any science images could be properly measured, they had to be corrected for noise. For this particular study, I utilized two different types of calibration images to accomplish this: Flat Field and Darks. Because Darks were taken at the same exposure rate and CCD temperature as the science images, the additional calibration image, known as Bias, was not included in the process.

For a CCD camera, the Quantum Efficiency (QE) is the measure of how much actual signal from incoming photons is translated into output. In a system running at a QE of 100%, all information from every photon would be collected and converted into output. In reality however, the QE of a camera varies across its pixel array. To compensate, flat field images, which can be taken a number of ways, including against the dome of the observatory or against the dusk or dawn sky, are applied to remove this variation (Howell, 2006).

CCD cameras also consist of thermally-related dark current noise (Mohsen et al., 1979). This means that at higher temperatures, additional electrons are freed in the structure of the CCD chip, and this in turn creates excess noise in the output imaging. To compensate for this, CCD cameras are cooled. Residual dark current interference is then removed with dark calibration frames. These are CCD images that are taken with the camera shutter closed and the device at the same temperature as it is during science imaging.

For all observations across all nights, sky flats, which are images taken against the background sky, were captured either at the beginning (dusk) or end (dawn) of each run, depending on the needs of the TOs. Dark images were obtained by me.

68347 (2001 KB67)

Data was obtained on June 3, 2018, June 4, 2018, and June 6, 2018. Time, weather, and moon phase for each observing night is reported in Table 2. All science images, across all nights, were taken at 120 second exposure times, with a 180 second pause between each image. Dark calibration images were also taken at 120 second exposure.

494999 (2010 JU39)

All exposures were taken at 100 seconds, with a 180 second pause in between each. All dark exposures were also taken for a duration of 100 seconds. The asteroid was tracked during the observation, allowing the stars to become trailed on all collected science images. Observing conditions are reported in Table 2.

455432 (2003 RP8)

The conditions for observations are reported in Table 2. Science exposures were taken at 60 second intervals, with a 180 second pause between each image. Darks were also taken at 60 second exposure times.

Data Calibration

Data calibration was completed using the computer program AstroImageJ, version 3.2.0. It was developed by Karen Collins and John Kielkopf, from the University of Louisville. In AstroImageJ, calibration is accomplished through the CCD Data Processor. This is a large sub window of the program that allows the user to combine raw calibration images into a single master. This means that either the median or average pixel values of each raw image are combined together into a single master image. For the current study, all dark calibration frames were median combined into a single master dark image, and all flat calibration frames were median combined into a single master flat image. Once this was completed, the program then subtracted the master dark image from the science image and divided the result by the master flat. This is represented by the following equation, which was modified from the one reported by Howell (2006, p. 85):

$$Calibration\ Image = \frac{Uncalibrated\ Image - Dark\ Frame}{Flat\ Frame}$$

As part of this process, the program created a sub folder for newly calibrated images that sat in the root directory where the original images were located.

The second and third nights of observations for 68347 (2001 KB67) were an exception to this calibration process. The script being used included the #CALIBRATE code that told the ACP software to use the already-obtained dark and flat images to automatically calibrate each science image. The results of this calibration matched that of calibration completed in the AstroImageJ software.

In addition to calibration, visual inspection was made of each set of images, for each night and for each asteroid, to ensure that they were oriented in the same direction. Changes in image orientation were the result of the German Equatorial Mount (GEM) Meridian flip. This

occurs when the GEM mounted telescope tracks an object from east to west across the sky. As it nears the Meridian, the scope stops to prevent elements of its hardware from hitting one another. It then rotates 180^0 in both RA and DEC, flipping the camera upside down with it, before reacquiring the target object. Any image with a view that was flipped upside down from the other images was reoriented using the AstroImageJ program. Further, all images were also inspected to make sure that objects and stars were visible and not obscured by light leaks, frost on the telescope lens, clouding, or any other outside interference or distortion.

Data Reduction

Photometric and Astrometric analysis was conducted using MPO Canopus version 10.7.11.1. This is a commercial software program designed by astronomer Brian D. Warner, and available through Bdw Publishing.

Aperture

In Canopus, the aperture is represented visually as three concentric circles, as depicted in Figure 1. The smallest inner aperture, known as the target aperture, encompasses the pixels of the targeted object(s). It is here that the value for the target is calculated. The target signal is found by subtracting out the averaged pixel values of the sky annulus from each individual pixel within the target aperture (Warner, 2012).

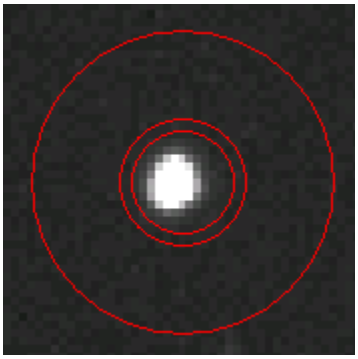

Fig. 1: Visual aperture used in MPO Canopus

The region that falls between the measuring aperture and the slightly larger circle that encompasses it is called a dead zone. No pixels within this boundary are measured. It is used as a barrier between the target and any stars or objects that may be close by. The area beyond the outer edge of the dead zone and encompassed by the outermost circle is described as the sky annulus (Warner, 2012).

Astrometry

Astrometric analysis was conducted on individual images for each asteroid. These were selected from across all nights of observation. For 68347 (2001 KB67), aperture settings of 11 width, 11 height, 2 dead, and 11 sky were used for photometry (abbreviated in Canopus as 11/11/2/11), and for astrometry. For both the photometry and astrometry of 494999 (2010 JU39) and 455432 (2003 RP8), the setting was 13/13/2/11.

In Canopus, astrometry is accomplished through chart-matching, which is done using the program's Automatch. For this feature, the program chooses two stars from an image and attempts to match them to their identical pairs on a chart. The chart is generated from an astrometric catalog. For this analysis, the MPOSC3 -2MASS Catalog, which consists of data derived from the Two Micron All Sky Survey (2MASS), was utilized. Once the matching process is accomplished, the software can then go on to identify the rest of the stars on the image, as well as the target object (Warner, 2011b).

For each asteroid in the current study, use of Automatch was affected by the orientation of the science images. For the first night of observation of 68347 (2001 KB67), and for all nights of observation of 494999 (2010 JU39), the telescope and camera had been rotated so the North and East alignments were not matched to the top and left side of the image, respectively. For these two asteroids, an adjustment was made on the charting page of the program's configuration

panel. It was specified that the CW = 240 so that it would better align with the science images. For 455432 (2003 RP8), the camera was not tilted on any night, so no adjustment had to be made.

In Canopus, once the Automatch is complete, astrometric information is available on the program's Reductions page. This includes the information for the target object, such as its name, its magnitude, its measured Signal-to-Noise Ratio (SNR), its measured position, both in RA and DEC and in X/Y coordinates for image position, and the error terms associated with the analysis. The software's goal is to compute an astrometric solution. This means that it matches the catalog positions of stars to their corresponding measured position on an image to provide an accurate mathematical model of the position of objects (Warner, 2011b). To do this, the program utilizes a maximum of 75 stars. For each star, its measured DEC and RA are displayed. The program color codes any star that has a derived DEC and RA that differs from what is found in the catalogue. For stars with a difference between 0.25 and 0.5 arcseconds, they are highlighted in green. For stars that differ between 0.5 and 0.75 arcseconds, they are shown in blue. And for any star with a difference greater than 0.75 arcseconds, a red highlight is used (Warner, 2012). For the current study, all highlighted stars were removed from the solution

Once a solution set has been finalized, the program allows for the results to be saved. For each individual image, results are converted into .AST file. A new .AST file is created for every analyzed image. Once the astrometric analysis has been completed for a set of images, the program combines the .AST files into a single report for submission to the Minor Planet Center (MPC) (Warner, 2012). The report contains the astronomer's contact and observatory information, the name of the observed object, the date of observation, and the object's RA and DEC for every image analyzed. For the current study, results were submitted to the MPC.

Calculation of Total Rate of Asteroid Motion

For each asteroid, two astrometric measurements taken from a single night were utilized to calculate the Total Rate of Motion (TRM). This was done by first noting the time, in seconds, between the two measurements. Then the Right Ascension (RA) and Declination (DEC) of both measurements were converted into degrees. For DEC, this conversion is represented mathematically by the following formula, where DD are degrees, MM are arcminutes, and SS are arcseconds:

$$DD + \frac{MM}{60} + SS/3600$$

Because RA is expressed in hours, minutes, and seconds, it must first be converted to decimal hours, as represented by the equation above, and then converted to degrees by multiplying by 15 (15^0 on the celestial sphere being the equivalent of 1 hour in RA).

The change in RA (ΔRA) was then calculated by subtracting the second measurement from the first. This process was also repeated to calculate the change in DEC (ΔDEC).

Geometrically, ΔRA and ΔDEC made up the horizontal and vertical sides, respectively, of a right triangle. By extension, the TRM of the asteroid was then found by performing a Pythagorean calculation for the length of the hypotenuse in degrees, converting that value it into arcseconds, and then dividing by the total elapsed duration, in hours. This resulted in a rate of motion that was measured in arc-seconds-per-hour (“/hr.).

For each object, TRM was calculated for each night. An averaged TRM was then calculated across all nights of observation, and the standard deviation was obtained to provide a measure of uncertainty.

Differential Photometry and The Lightcurve Wizard

Differential Photometry in MPO Canopus is done, in part, through the software's light curve wizard. This feature allows the science images to be grouped and analyzed in sessions. For each session, all the images need to contain both the target object and the same background field of stars that can be used for comparison.

For the current research, all three of the asteroids moved rapidly across the night sky, and the background stars changed multiple times in a single night of observation. Because of this, each science image needed to be carefully analyzed and grouped with an appropriate set of comparable images.

To accomplish this, Canopus's Blinker page was utilized. This feature allows for images to be placed in succession and shown rapidly, one after another. This results in the background stars remaining stationary while the target asteroid is seen moving across the sequence (Warner,2012). In the current study, groups of images were loaded into the Blinker. A reference star was selected that was present on each image used. It allowed the program to align the images to create a stable sequence. I would then run the sequence, noting how the background stars changed over its duration. For any image where the change of backgrounds was drastic, it was pulled for inclusion in the next session.

To create a session, I would Automatch the first image to be included. This allowed the software to automatically establish the date and time of observation so that it would not have to be entered manually. For each session made, the object, and the filter and equipment used, had to be specified.

Once a session was created, I would then engage the Lightcurve Wizard. The initial step in this process was to load the first image of the session. While doing so, a small box for star

subtraction would be checked. Additional details on this selection and its use will be described below.

With the first image loaded, the position of the asteroid was identified. This was done through a menu option that allows the user to select the name of the target object from MPC Small Body Catalog. Once it is selected, the software shows its location and projected path on the image.

After identifying the asteroid, the Comp Star Selector was used to pick four comparison stars, including the anchor star (the first comparison star chosen) that is vital in the photometry process and critically important to other functions in Canopus as well. The selector provides a plot of the magnitudes of all the background stars identified during the Automatch. It superimposes a slope line over the data and provides a numerical measure of standard deviation. It also allows a user to filter the plot so that only solar-color stars, which are similar to the color of an asteroid, are displayed (Warner, 2012). For the current study, only solar-color comparison stars were used. Figure 2 provides an example of the Comp Star plot and menu window.

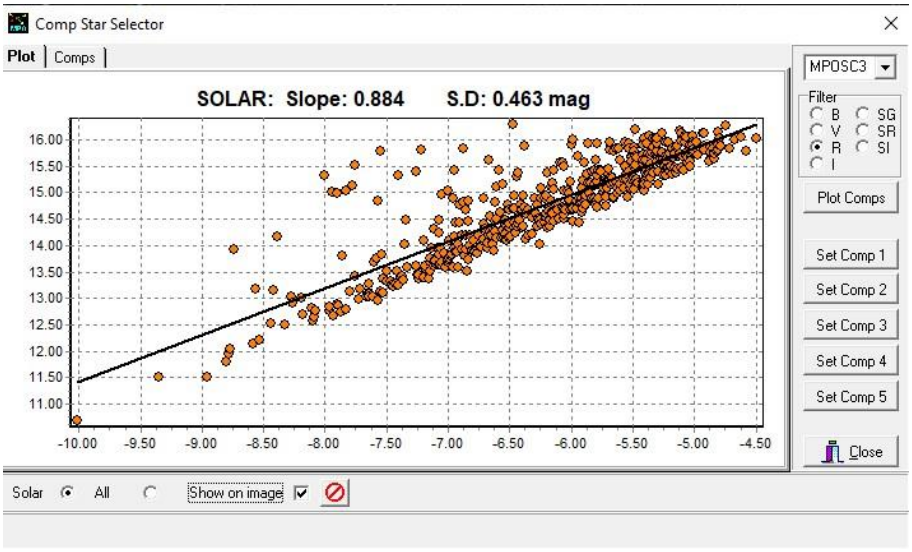

Fig. 2: Example of the Comp Star Selector in MPO Canopus

In addition to color, other factors were chosen based on criteria outlined by Warner (2012). This included how close the star fell to the slope line, how well it was separated from any nearby stars, how close it was to the target, and whether or not it fell along the direction of the motion of the asteroid. It was also an absolute requirement that each comparison star appeared in all session images.

After the comparison stars are chosen, the Lightcurve Wizard asks the user to load a second session image. It then uses this to calculate the asteroid's movement rate, as well as any amount of image rotation that may exist in the overall session set. Once the image is loaded, the program requires the user to identify the previously chosen comparison stars and the target asteroid again. Therefore, it is critical that the image being used contains all the comparison objects, and that the anchor not be near the extreme edges (Warner, 2012). For the current study, the final image in each session was always utilized.

Once the second image is processed through, the program then reloads the first image and initiates the star subtraction feature, StarBGone. StarBGone places a red line along the path of the asteroid, highlighting where it will travel through the subsequent session images. It allows the user to remove stars that sit on or along this path so that they will not add interference into the final analysis. Overall, it can be effective in removing excess noise. However, as Warner (2011b) points out, StarBGone cannot eliminate distortion from stars with significantly brighter magnitudes than that of the target object.

As part of the subtraction process, Canopus asks for two reference stars to be selected. As Warner (2012, pp.79) states: "As each image is opened, Canopus finds Reference Star 1 and scales it to match each subtraction star in proportion to its relative brightness to the reference star on the original image. The scaling is done on several levels in order to get the best possible

match, i.e. total intensity and the contribution of each pixel to the total intensity. This allows Canopus to do a good match on images that are trailed as well as perfectly guided."

The first reference star is usually one of the comparison stars. For the current analysis, the second comparison star was always chosen. The second reference star was chosen based on criteria detailed in Warner (2012). It had to appear in all session images, it needed to be non-saturated, and it needed to have separation from other stars.

After selecting appropriate reference stars, the user traces over the asteroid's path line, and selects any stars that are on or near it to be added to a removal list. In the current research, this process was done for every session.

Once the subtraction selection is completed, the Lightcurve Wizard moves to the final steps of the process. It allows the user to save a copy of the first image, with the comp stars clearly labeled for reference. Then it asks for all the images included in the session to be selected, before opening the Canopus Image List window.

Differential Photometry and the Canopus Image List

The Canopus Image List is where each image is processed to find the differential magnitude between the target and its comparisons. To calculate the differential magnitude, the program utilizes the instrumental magnitude of the asteroid, and subtracts from it the average instrumental magnitude of the comparison stars (no average is used if there is only one comparison star in the analysis).

In general, an instrumental magnitude is derived from the image itself. In other words, it is the magnitude as measured through the instrument used and recorded on the image taken. The value is found through the following equation, where F represents the amount of flux from an object (Warner, 2016):

$$m = -2.5 * Log_{10}(F)$$

For the computation of differential magnitude (Δm), Canopus uses the following formula (Warner, 2012):

$$\Delta m = (m_t - m_c) + T_r(CI_t - CI_c) + (Z_t - Z_c)$$

In the above equation, m_t is the instrumental magnitude of the target asteroid, m_c is the instrumental magnitude of the comparison stars (or an average if more than one comparison star is utilized), T_r is the transform coefficient for the R filter, CI_t is the color index taken from a standard catalog for the target, $CI_c$is the color index for the comparison star (averaged for more than one comparison) , and Z_t and Z_c represent the zero point offset for the target and comparison, respectively. The Z values for both the target and the comparison stars during a single night are the same, and therefore the difference is 0, effectively removing them from the calculation (Warner, 2012).

For the current study, I took advantage of an option in the MPO Canopus configuration panel that allows for derived magnitudes to be used in the calculation. Derived magnitudes represent a fusion between the method that uses instrumental magnitude (represented in the equation above,), and the method that relies solely on catalog magnitudes. In this approach, the catalog magnitude for the comparison star, M_c, is added to the value for $(m_t - m_c)$ (Warner, 2012).

The process described above occurs out-of-sight to the software user. The Canopus Image List itself loads a listing of all the session images into a single window. The user is then given several options to choose from regarding how each image is measured. In the full manual mode, the program identifies both the target asteroid and the comparison stars by highlighting

them with apertures, and then asks the user to accept the placement. This is done for each image (Warner, 2012).

In the Semi-Auto mode, the user is asked if the images should be simple matched, or full auto matched. If the Simple Matched preference is chosen, then the program will identify the target and comparisons in each image, but it will not ask the user to accept the findings for each image. Instead it will move to the subsequent images, identifying the target and comparisons in each, until all images have been processed. If any issue with aperture placement on an image occurs, the program will stop the analysis and display an error window that allows the user to either resolve the issue or move on to the next image. In contrast, Full Auto Matched mode forces automatic matching to occur, and it will not display any error to the user (Warner, 2012).

The current study utilized the Semi-Auto mode option, and I did not manually accept aperture placement each time an image was analyzed but did receive warning messages if the target and/or comparison stars could not be matched.

Comparison Star Check

Before undertaking period analysis, all comparison stars for each session, and each asteroid, were checked to determine if a variable star had accidentally been included in the analysis. In Canopus, this is done through the Photometry Sessions Data window, and on the Comparison Plots and Catalog Check Tabs.

On the Comparison Plots tab, the user can look at each comparison star individually. It is expected that all points in the star's plot form a relatively flat pattern. If they show variability that indicates a sinusoidal curve, then the star is likely variable, and should be excluded from the analysis.

On the Catalog Check tab, the individual stars are plotted on top of one another. The patterns should lay close to each other. If there is significant separation in one or more plot, then the star should be excluded.

For the current analysis, all suspected variables, and any star(s) separated from the others on the catalog plot, were excluded.

Light Curve and Period Analysis

In Canopus, all period determinations are done through the Lightcurve Analysis page. It is here that the program uses the Fourier Analysis for Lightcurves (FALC) to find an object's rate of rotation (Warner, 2012). FALC was originally developed by Harris et al. (1989), who were the first to use it by analyzing the period of five asteroids that had been observed over six years.

Buchheim (2007) notes that the Fourier analysis performed by FALC attempts to find the light curve best fitting the data by examining all known period solutions simultaneously. He describes the mathematical process in detail:

> *"*Assume that the lightcurve is described by an equation of the form:
>
> $$M(t.P) = a_0 \sum_{i=1}^{n} [a_i \sin\left(\frac{2\pi t}{P}\right) + b_1 \cos\left(2\pi t/P\right)]$$
>
> Where t is the time, P is the period, and n is the 'order' of the Fourier fit to the data. Take that equation and your measured differential photometry…pick a starting value of P and perform a least-squares analysis to determine the values of a_i and b_1 that give the best fit to the data. Calculate the resulting mean-square error between your data and the best-fit equation $M(t)$. Then increment P by a small amount (to $P + \Delta P$), and repeat the least-squares analysis and the calculation of the mean-square error for this new period

estimate. Do that a zillion times, until you find the period estimate that minimizes the mean-square error. That's your best-estimate period P*."

In practical terms, Canopus looks at all possible solutions to the data. Potential periods are displayed in two ways, with both being available through the Period Spectrum window. The first, as shown in Figure 3, is a visual graph that plots the RMS error of solutions (on the Y-axis), against the time of the period as measured in hours or days (plotted on the X axis). For more likely periods, the plot will dip close to the X axis, indicating smaller amounts of error that correspond to the given time.

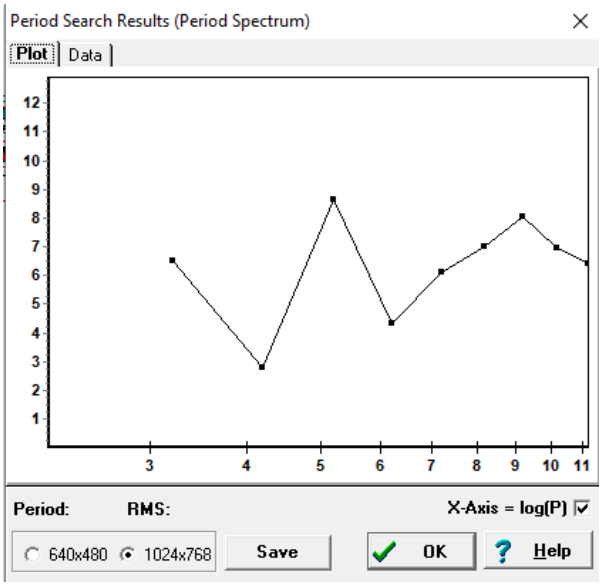

Fig. 3: Example of a Period Spectrum Graph in MPO Canopus

A table of numerical RMS values with corresponding period solutions, as shown in Figure 4, is also displayed through a tab in the Period Spectrum window. This provides the same information as the RMS/Period graph and shows the error values that correspond to a variety of possible solutions. The lower the error, the more likely the correct solution (Warner, 2012).

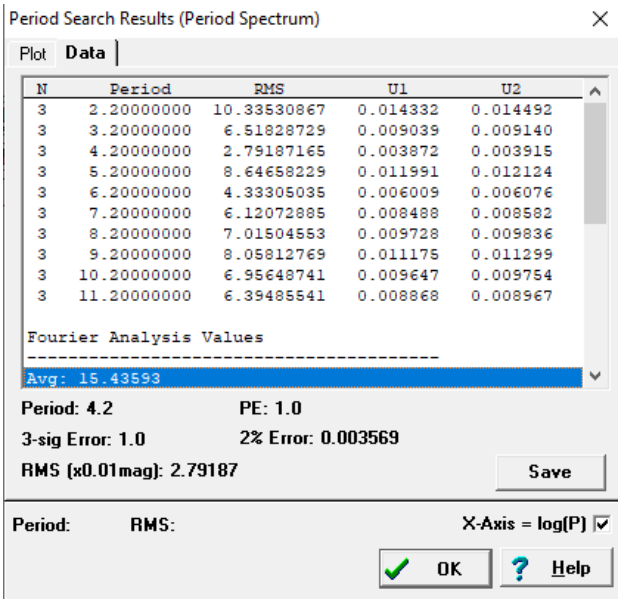

Fig. 4: Example of a Period Spectrum Table

In addition, the table produces three other error terms. Warner (2012, pp. 100) defines these as follows:

> "PE (Probable Error): This is the error directly out of the Fourier analysis. It is often 'too optimistic'; 3-sig Error: This is the 3-sigma error, i.e. 3x the probable error and more conservative and one often quoted; 2% Error: This is the error that would cause the last data point in the set (by date order) to be shifted by 2% (or, an error of about 7^0 rotation). It uses a formula similar to the one used to estimate the period error when doing spin and shape axis modeling."

For the purposes of the current study, both RMS and the 3-sig Error were utilized.

The program uses a period search engine that allows the user to test and modify solutions by adjusting a set of parameters. More specifically, these parameters include: *Orders*, which specifies the number of harmonic orders used; *Min.*, which sets the minimum amount of time, usually in hours, for the period; *Size*, which sets the time of each step in the analysis by either hours or days; *Steps*, which sets the amount of steps specified for the search; *Bin*, which specifies

the number of data points that will be combined into a single data point; and *Max Diff*, which specifies how much difference there will be between each pair of data points (Warner, 2012).

In addition, the user can also choose the type of search conducted by the period engine. The three choices available are: *Period (reg)*, *Orders*, and *Period (auto)*. For *Period (reg)*, the values provided by the user in the *Orders*, *Min.*, *Size*, and *Steps* parameters are utilized as entered, with no modification by the program. For *Orders*, the search adjusts the number of orders so that it corresponds to the lowest RMS values that would occur if the period were held constant. And for *Period (auto)*, the search uses a step size that adjusts according to the preliminary period, and according to amount of time, measured by days, that the data covers (Warner, 2011b). For the current study, *Period (auto)* was utilized during the analysis.

Canopus also gives additional options for data plotting. With the *Raw* option, the program will plot the differential magnitudes against the Julian date when they were collected; With *Fourier*, it places a curve over the data points. And with *Transforms*, the software can check to see if any corrections for color index and/or extinction are being used (Warner, 2011b).

For the current study, the *Raw* option was used as a check of the raw data for individual sessions. This allowed for screening of any outlier points, and such points were removed from the data before the analysis continued.

The *Fourier* option was also used, and a curve was placed across the data for all three asteroids. According to Warner (2012), the Lightcurves of asteroids are often bimodal, meaning that they have two peaks (maximums), and two lows (minimums). Adding a visual curve to the data allowed for this pattern to be better recognized and refined.

After the raw data from each session was inspected, the period search began. I set the initial parameters to include six orders, a min. of 2.0, a size of 1.0, ten steps, and a max. diff also

of ten. The bin option was always kept at 1 for each target. This generated an initial period spectrum. From this, a trial and error process was used as potential period solutions were investigated.

To home in on a specific period solution for each asteroid, I tried different combinations of settings in the parameters of the period search engine, as discussed above. However, rarely did these modifications result immediately in a refined light curve. Often data from one session would appear high above or below data from the other sessions, producing an inaccurate or skewed lightcurve.

However, Canopus provides a way to correct for this. When each solution is processed, the program pops up a new Period Spectrum window, as well as a separate window called the Comp Adjust Form. This form allows the user to adjust the Deltacomp values for individual sessions. This, in turn, moves the data points from the selected session vertically, and aligns it with the other sessions (Warner, 2011b). For the current study, the Comp Adjust Form was utilized to place data from each session tightly around the light curve.

As a final step, any data point from any session that fell well above or below the curve was deleted. This allowed the remaining data to wrap closer to the curve, providing for a more accurate solution.

Asteroid Size Estimation

To calculate the effective diameter (D_{eff}) of each asteroid, the following equation, reported originally by Fowler & Chillemi (1992), was used, where Pv is the geometric albedo, and H is the absolute magnitude:

$$D_{eff} = \left[\frac{1329}{(Pv)^{\frac{1}{2}}}\right] * 10^{-(\frac{H}{5})}$$

As of the writing of this thesis, no formal measure of albedo had been reported for any of the target asteroids. However, The Asteroid Lightcurve Database (LCDB) (Warner, 2011) lists an estimated albedo for each of the target objects at 0.2. Warner (personal communication, February 11, 2021) clarified that because none of the asteroids observed for this thesis had been included in IR surveys or given taxonomic classifications, the albedo estimation of 0.2 ± 0.07 associated with S and Q-type asteroids was included in the objects' entry as part of the procedure outlined by Warner et al. (2009). Further, Warner (personal communication, February 11, 2021) stated that the magnitudes for each asteroid were taken from the MPCORB, and each had an uncertainty of roughly ± 0.1.

Three diameters were determined for each asteroid using the formula reported above. The first diameter was calculated with the given albedo and magnitude information. The other two calculations reflected the albedo and magnitudes with their lower and upper uncertainties factored in. Once obtained, the three diameter values were averaged, and a standard deviation was calculated. This provided a single estimate with an upper and lower uncertainty limit.

CHAPTER THREE

RESULTS

68347 (2001 KB67)

Astrometry was conducted by measuring two images from each night. The results are recorded in Table 3. The TRM was calculated as 518.855 ± 141.000 "/hr.

Table 3: Astrometric Observations for 68347 (2001 KB67)

Date (UTC)	RA (J2000.0)	DEC (J2000.0)
2018 06 04.20155	17 31 25.34	+30 14 47.1
2018 06 04.36477	17 28 33.81	+30 02 20.7
2018 06 05.17895	17 16 51.03	+29 02 39.2
2018 06 05.33819	17 14 41.64	+28 52 00.1
2018 06 07.28537	16 55 11.38	+26 58 18.2
2018 06 07.34321	16 54 41.98	+26 55 20.9

As part of the period analysis, all comparison stars were examined to detect for the inclusion of variables, as outlined above. In total, four comparisons were removed from across the sessions

Figure 5 shows the phased plot of the light curve for 68347 (2001 KB67). It was derived with a third harmonic order and was found to be 6.350 ± 0.045 hrs., with an amplitude of 0.24 magnitude. The RMS was 3.66, with a 3-sig Error of 0.04.

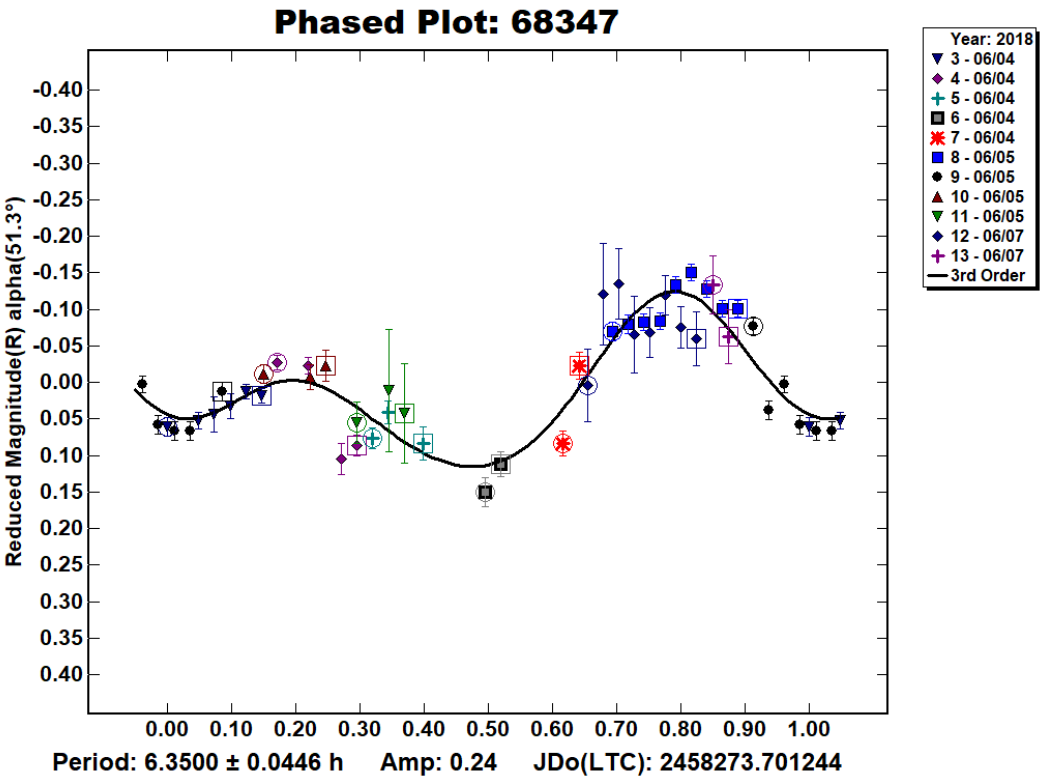

Fig. 5: Phased Plot for 68347 (2001 KB67)

The calculated effective diameter for the asteroid was 324 m (0.324 km) ± 61.225 m (.0623 km), a value smaller than the estimate given by Warner (2018).

494999 (2010 JU39)

Astrometric measurements were performed on three images from the first night, and on three images from the second night, as reported in Table 4. The TRM was calculated based on the first and last entry for each night. It measured at 1651.147 ± 100.897 "/hr.

Table 4: Astrometric Observations for 494999 (2010 JU39)

Date (UTC)	RA (J2000.0)	DEC (J2000.0)
2019 06 26.19990	15 44 45.80	+20 29 12.4
2019 06 26.24397	15 42 59.80	+20 23 01.2

2019 06 26.28679	15 41 16.25	+20 16 50.2
2019 06 27.16402	15 04 29.91	+17 48 00.5
2019 06 27.22670	15 01 42.21	+17 35 29.8
2019 06 27.29082	14 59 18.56	+17 24 37.2

For photometric analysis, three comparison stars were removed from across the sessions. Figure 6. Reports the Phased Plot for 494999 (2010 JU39). It was found using a third harmonic order and revealed a period of 2.278 ± 0.016 hrs, with an amplitude of 0.13 magnitude. The RMS was 2.45 and a 3-sig Error of 0.02.

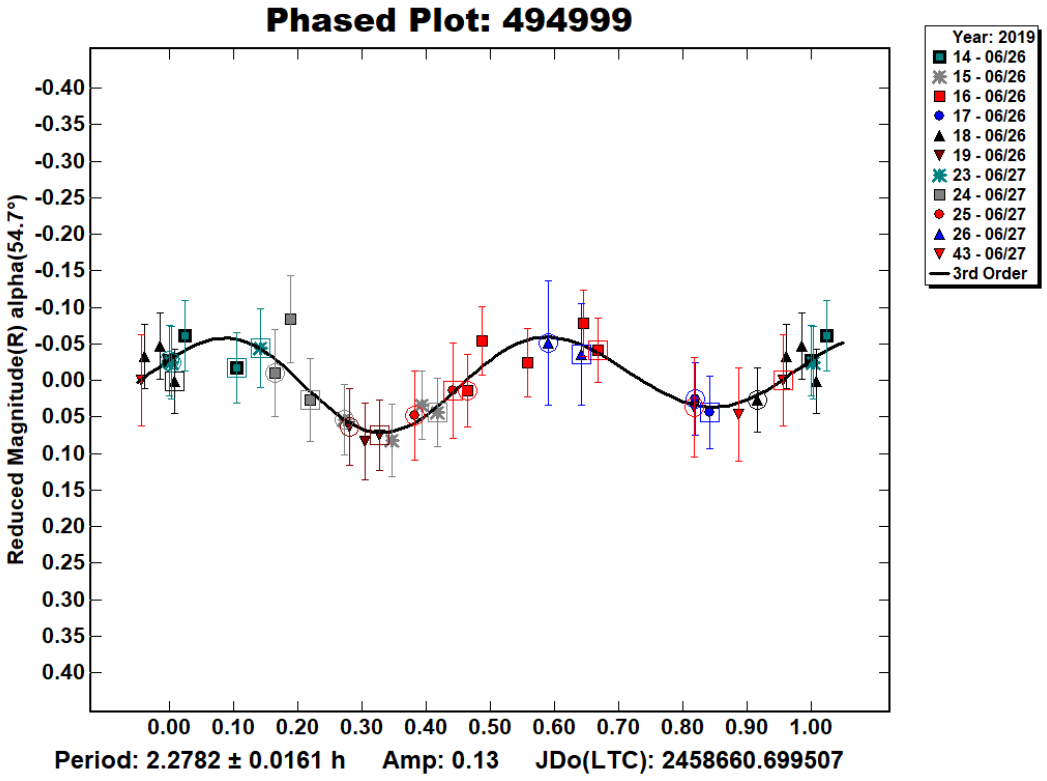

Fig. 6: Phased Plot for 494999 (2010 JU39)

The effective diameter of the asteroid was calculated as being 355 m (0.355 km) ± 67.132 m (.067 km).

455432 (2003 RP8)

Astrometric information for 455432 (2003 RP8) is reported in Table 5. Measurement was taken from two images per each night of observation. The TRM was calculated as 665.331 ± 81.244 ”/hr.

Table 5: Astrometric Observations for 455432 (2003 RP8)

Date (UTC)	RA (J2000.0)	DEC (J2000.0)
2019 07 30.18791	19 19 56.38	+01 53 31.5
2019 07 30.31696	19 19 14.15	+02 30 21.2
2019 07 31.17451	19 15 01.80	+06 28 26.4
2019 07 31.30336	19 14 21.14	+07 03 02.3
2019 08 03.16531	19 01 42.19	+18 28 57.9
2019 08 03.18978	19 01 20.92	+18 45 38.5

For the photometric analysis, ten comparison stars were excluded from across the twelve data sessions. Figure 7 shows the phased plot for 455432 (2003 RP8). The period was determined with a third harmonic order and was found to be 4.200 ± 0.015 hrs, with an amplitude of 0.30 magnitude. The RMS was 2.79 and 3-sig Error of 0.01.

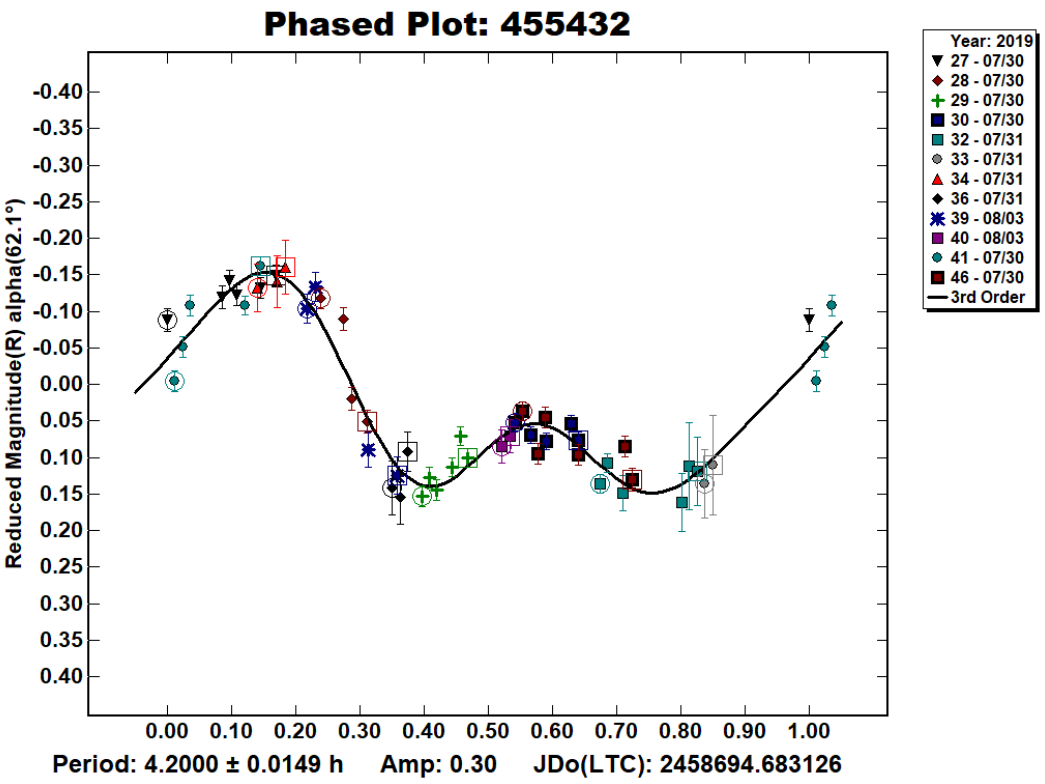

Fig. 7: Phased Plot for 455432 (2003 RP8)

The effective diameter of the asteroid was found to be approximately 708 m (0.708 km) ± 133.946 m (0.134 km).

CHAPTER 4

CONCLUSIONS

The current study focused on the astrometry and photometry of near-Earth objects 68347 (2001 KB67), 494999 (2010 JU39), and 455432 (2003 RP8). At the time of data collection, neither a previously derived rotational period, nor a significant body of research, had been published for any of the target asteroids

The period obtained for 68347 (2001 KB67) matched well to that found by both Warner (2018), and Loera-Gonzalez et al. (2019). The calculated average effective diameter matched the estimate reported by Warner (2018).

The approximate rotational rate derived for 455432 (2003 RP8) corresponded closely to the estimations given by Warner & Stephens (2020). Further, the derived light curve also showed the same type of asymmetry, attributed to a high phase angle, that was originally noted by Warner & Stephens (2020). The phase angle during my observation was 62.1^0. The only difference to note was in calculated effective diameters. For my study, I found an average diameter of 708 m (0.708km) ± 133.946 m (0.134 km), as contrasted to the 680 m (with no reported uncertainty) determined by Warner & Stephens (2020).

The period for 494999 (2010 JU39) differed significantly from that found by Warner & Stephens (2019). The original published rotation, based on an incomplete light curve, revealed the object to be a slow rotator, with a rate of over 30 hours. The current findings, however, indicated the opposite, showing the asteroid to be rotating rapidly at around 2.28 hrs. With an approximate average effective diameter of 355 m (0.355 km) ± 67.132 m (.067 km), either scenario is theoretically possible. The shorter rotation still falls above the break-up limit for asteroids of that size, and longer spin is also not uncommon within that population.

Some major limitations to the current research may have influenced the reported results. Weather, for example, was often problematic during data collection, with several nights being rained out, and others being limited in viewing due to cloud cover. Furthermore, technical glitches, especially experienced during the observation of 494999 (2010 JU39) put a limit to the amount of data that could be collected.

Magnitude also proved to be a controlling factor. Because the telescope was limited to a magnitude of 16, the number of nights available to observe were often truncated.

The observations for 494999 (2010 JU39) presented even more additional issues. The asteroid was only visible in the sky for a few brief nights, so viewing availability was shortened. Also, during observing I tracked the asteroid and allowed the stars to be trailed. This cut down on the number of viable comparison stars that were available during analysis. This problem persisted even when different size apertures were used for data reduction, and this may have affected both the astrometry and photometry.

All three of the presented light curves also suffer from a scarcity of data. Because all observations were limited in duration, and because data had to be trimmed during final analysis to find the best fit for each light curve, only a small amount of the data points were utilized.

Because the periods of 68347 (2001 KB67) and 455432 (2003 RP8) have seemingly been resolved, future research should focus on 494999 (2010 JU39). Due to the limited viewing window for this object's 2019 flyby, there is still enormous uncertainty about its true rotational rate. Further observation to clarify its spin rate should be undertaken.

REFERENCES

Al-Sufi (2018). *Kitab suwar al-kawakib*. World Digital Library. https://dl.wdl.org/2484/service/2484.pdf.

Alvarez, L.W., Alvarez, W., Asaro, F., & Michel, H.V. (1980). Extraterrestrial cause for the Cretaceous-Tertiary extinction. *Science*, 208, 1095-1108.

Bancelin, D., Hestroffer, D., & Thuillot, W. (2012). Dynamics of asteroids and near-Earth objects from Gaia astrometry. *Planetary and Space Science*, 73, 21-29.

Bell, J.E., Keil, K. (1987, March 16-20). Spectral alteration effects in chondritic gas-rich breccias: Implications for S-Class and Q-class asteroids. [Paper presentation]. In Lunar 10851 01-91). *Lunar and Planetary Science Conference*, Houston, TX (pp. 573-580). Cambridge University Press/Lunar and Planetary Institute.

Belton, M.J.S., Veverka, J., Thomas, P., Helfenstein, P., Simonelli, D., Chapman, C., Davies, M.E., Greeley, R., Greenberg, R. Head, J., Murchie, S., Klassen, K., Johnson, T.V., McEwen, A., Morrison, A., Morrison, D., Neukum, G., Fanale, F., Anger, C., …& Pilcher, C., (1992). Galileo encounter with 951 Gaspra: First pictures of an asteroid. *Science*, 2587, 1647-1652.

Binzel, R.P., Bus, S.J., Burbine, T.H., & Sunshine, J.M. (1996) Spectral properties of near-Earth asteroids: Evidence for sources of ordinary chondrite meteorites. *Science*, 273, 946-948.

Binzel, R.P., Rivkin, A.S., Stuart, J.S., Harris, A.W., Bus, S.J., & Burbine, T.H. (2004). Observed spectral properties of near-Earth objects: results for population distribution, source regions, and space weathering processes. *Icarus*, 170, 259-294.

Binzel, R.P., Reddy, V., & Dunn, T. (2015) The Near-Earth Object Population:

Connections to Comets, Main-Belt Asteroids, and Meteorites. In Michel, P., DeMeo, F. E., & Bottke, W.F. (Eds.) *Asteroids IV* (pp. 243-256). Tucson, Az: The University of Arizona Press.

Binzel, R.P., DeMeo, F.E., Turtelboom, E.V., Bus, S.J., Tokunaga, A., Burbine, T.H., Lantz, C., Polishook, D., Carry, B., Morbidelli, A., Birlan, M., Vernazza, P., Burt, B.J., Moskovitz, N., Slivan, S.M., Thomas, C.A., Rivkin, A.S., Hicks, M.D., Dunn, T., … & Kohout, T. (2019). Compositional distributions and evolutionary processes for the near-Earth object population: Result from the MIT-Hawaii Near-Earth Object Spectroscopic Survey (MITHNEOS). *Icarus*, 324, 41-76.

Borovicka, J., Spurny, P., Brown, P., Wiegert, P., Kalenda, P., Clark, D., and Shrbeny, L. (2013). The trajectory, structure, and origin of the Chelyabinsk asteroidal impactor. *Nature*, 503, 235-247.

Bottke, W>F., Morbidelli, A., Jedicke, R., Petit, J-M., Levison, H.F., Michel, P., & Metcatfe, T.S. (2002). Debiased orbital and absolute magnitude distribution of the near-Earth objects. *Icarus*, 156, 399-433.

Bottke, W.F., Vokrouhlicky, D., Rubincam, D. P., & Nesvorny, D. (2006) The Yarkovsky and YORP Effects: Implications for asteroid dynamics. *The Annual Review of Earth and Planetary Science*, 34, 157-191.

Boyle, W.S., & Smith, G.E. (1970). Charge coupled semiconductor devices. *Bell System Technical Journal,* 52, 587-593.

Buchheim, R.K. (2007). *The sky is your laboratory: Advanced astronomy projects for amateurs*. Chichester, UK: Praxis Publishing Ltd.

Bus, S. J., & Binzel, R.P. (2002) Phase II of the Small Main-Belt Asteroid Spectroscopic

Survey. *Icarus*, 158, 146.177.

Cellino, A., Bus, S. J., Doressoundiram, A., & Lazzaro, D. (2002) Spectroscopic Properties of Asteroid Families. In Bottke Jr., W.F., Cellino, A., Paolicchi, P., Binzel, R.P. (Eds.) *Asteroids III:* (pp. 633–643). Tucson, Az: The University of Arizona Press.

Chang, C-K., Waszczak, A., Lin, H-W., & Ip, W-H., Prince, T.A., Kulkarni, S.R., Laher, R., & Surace, J. (2014). A new large super-fast rotator: (335433) 2005 UW163. *The Astrophysical Journal Letters*, 791, L35.

Chang, C-K, Lin, H-W, Ip, W-H., Prince, T.A., Kulkarni, S.R., Levitan, D., Laher, R. & Surace, J. (2016). Large super-fast rotator hunting using the intermediate Palomar transient factory. *The Astrophysical Journal Supplement Series*, 227, 1-13.

Chapman, C. R., & Salisbury, J.W. (1973). Comparisons of meteorite and asteroid spectral reflectiveness. *Icarus*, 19, 507-622.

Copernicus, N. (1995). *On the Revolution of the Celestial Spheres*. (C.G. Wallis, Trans.). Amherst, NY: Prometheus Books. (Original work published 1543).

Chesley, S.R. Ostro, S.J., Vokrouhlicky, D., Capek, D., Glorgini, J.D., Nolan, M.C., Margo, J-L., Hine, A.A., Benner, L.A.M., & Chamberlion, A.B. (2003). *Science*, 302, 1739-1742.

Chodas, P. (2019) *NEO Earth Close Approaches*. Center for Near Earth Object Studies. https://cneos.jpl.nasa.gov/ca/.

Chodas, P. (2012) *NEO Basics*. Center for Near Earth Object Studies. https://cneos.jpl.nasa.gov/about/neo_groups.html

Cuk, M. (2007) Formation and destruction of small binary asteroids. *The Astrophysical Journal*, 659, L57-L60.

Dawes, W.R. (1851). On a photometrical method of determining the magnitude of telescopic

stars. *Monthly Notices of the Royal Astronomical Society*, XI, 187-190.

Desmars, J., Bancelin, D., Hestroffer, D., & Thuillot, W. (2013). Statistical and numerical study of asteroid orbital uncertainty. *Astronomy & Astrophysics*, 554, A32.

DeMeo, F., & Binzel, R.P. (2007) Comets in the near-Earth object population. *Icarus*, 194, 436-449.

DeMeo, F. E., Binzel, R. P. Slivan, S. M., & Bus, S. J. (2009) An extension of the Bus asteroid taxonomy into the near-infrared. *Icarus*, 202, 160–180.

Dunn, T. L., Burbine, T.H., Bottke, W.F., & Clark, J.P. (2013). Mineralogies and source regions of near-Earth asteroids. *Icarus*, 222, 273-282.

Durech, J., Vokrouhlicky, D., Pravec, P., Hanus, J., Farnocchia, D., Krugly, Y. N., Ayvazian, V.R., Fatka, P., Chiorny, V.G., Gaftonyuk, N., Galad, A., Groom, R., Hornoch, K., Inasaridze, R.Y., Kucakova, H., Kusnirak, P., Lehky, M., Kvaratskhelia, O.I., Masi, G., … & Warner, B.D. (2018) YORP and Yarkovsky effects in asteroids (1685) Toro, (2100 Ra-Shalom, (3103) Eger, and (161989) Cacus. *Astronomy & Astrophysics*, 609, Retrieved from https://www.aanda.org/articles/aa/abs/2018/01/aa31465-17/aa31465-17.html

Eggl, S., Ivantsov, A., Hestroffer, D., Perna, D., Bancelin, D., & Thuillot, W. (2013). High precision astrometry in asteroid mitigation – the Neoshield perspective. In Cabresy, L., Martins, F., Nuss, E., Palacios, A. (Eds.) *Proceedings of the annual meeting of the French Society of Astronomy & Astrophysics*: (pp. 169–176). Montpellier, France: Société Francaise d'Astronomie et d'Astrophysique.

ESA (2019, September 1). *Summary*. Retrieved from https://sci.esa.int/web/gaia/-/28820-summary

Einstein, A. (1905). Uber einen die Erzeugung und Verwandlung des Lichtes betreffenden heuristischen Gesichtspunkt (On a heuristic point of view about the creation and conversion of light). *Annalen der Physik*, 17, 132-148.

Feierberg, M.A., Larson, H.P., & Chapman, C.R. (1982). Spectroscopic evidence for undifferentiated S-type asteroids. *The Astrophysical Journal*, 257, 361-372.

ESA (2019, September 1). *Summary*. ESA Science and Technology. https://sci.esa.int/web/gaia/-/28820-summary

Fieber-Beyer, S.K, Gaffey, M.J., Bottke, W.F., & Hardersen, P.S. (2015). Potentially hazardous asteroid 2007 LE: Compositional link to the black chondrite Rose City and asteroid (6) Hebe. *Icarus*, 250, 430-437.

Fieber-Beyer, S.K., & Gaffey, M.J. (2019). NEA 162385 (2000 BM19): Near-infrared compositional analysis of a mining target. *Icarus*, 328, 23-31.

Fowler, J.W., & Chillemi, J.R. (1992). IRAS asteroid data processing. In Tedesco, E.F. (Ed.) *The IRAS Minor Planet Survey, Tech. Rep. PL-TR-92–2049*, pp. 17-43, Hanscom AF Base, MA.

Gaffey, M.J. (1984). Rotational spectral variations of asteroid (8) Flora: implications for the nature of the S-type asteroids and for the parent bodies of ordinary chondrites. *Icarus*, 60, 83-114.

Gaffey, M. J., Bell, J.F., & Brown, R.H. (1993) Mineralogical Variations within the S-Type asteroid class. *Icarus*, 106, 573-602.

Galache, J.L., Beeson, C.L., McLeod, K.K., & Elvis, M. (2015). The need for speed in near-Earth asteroid characterization. *Planetary and Space Science*, 111, 155-166.

Galilei G. (1989*). Sidereus Nuncius* (A. van Helden, Trans), Chicago, IL: University of Chicago

Press (Original work published 1610).

Granvik, M., & Brown, P. (2018) Identification of meteorite source regions in the solar system. *Icarus*, 311, 271-287.

Gunn, J.E., Siegmund, W.A., Mannery, E.J., Owen, R.E., Hull, C.L., Leger, R.F., Carey, L.N., Knapp, G.R., York, D.G., Boroski, W.N., Kent, S.M., Lupton, R.H., Rockosi, C.M., Evans, M.L., Waddell, P., Anderson, J.E., Annis, J., Barentine, J.C., Bartoszek, L.M, … & Wang, S-I. (2006). The 2.5 m telescope of the Sloan Digital Sky Survey. *The Astronomical Journal*, 131, 2332-2359.

Hallwachs, W. (1888). Ueber den einfluss des lichtes auf electrostatisch geladene korper. *Annalen de Physik*, 209, 301-312.

Harris, A.W., & Burns, J.A. (1979). Tabulation and analysis of rates, pole positions, and shapes. *Icarus*, 40, 115-144.

Harris, A.W., Young, J.W., Bowell, E., Martin, J. Millis, L., Poutanen, M., Scaltriti, F., Zappal, V., Schober, H.J., Debehogne, H., & Zeigler, K.W. (1989). Photoelectric observations of asteroids 3, 24, 60, 261, and 863. *Icarus*, 77, 171-186.

Harris, A.W. (1996) The rotation rates of very small asteroids: Evidence for "rubble pile" structure. *Lunar and Planetary Science*, 27, 493.

Harris, A.W., & D'Abramo, G. (2015) The population of near-Earth asteroids. *Icarus*, 257, 302-312.

Hergenrother, C.W., & Whitely, R. J. (2011) A survey of small fast rotating asteroids among the near-Earth asteroid population. *Icarus*, 214, 194-209.

Herschel, W. (1796). On the method of observing the changes that happen to the fixed stars; with

some remarks on the stability of the light of our Sun. To which is added, a catalogue of comparative brightness, for ascertaining the permanency of the lustre of stars. In *The scientific papers of Sir William Herschel* (530-545) London, England: The Royal Society.

Hertz, H. (1887). Ueber einen einfluss des ultravioletten lichtes auf die electrische entladung. *Annalen der Physick*, 267, 983-1000.

Hipparchus (1894). *In Arati et Eudoxi phaenomena commentariorum*. (K. Manitius, Trans.). Leipzig, Germany, Lipsiae. (Original work published 126 BC).

Hildebrand, A.R., Penfield, G.T., Kring, D.A., Pilkington, M., Camargo, A.Z., Jacobsen, S.B., & Boynton, W.V. (1991). Chicxulub Crater: A possible Cretaceous/Tertiary boundary impact crater on the Yucatan Peninsula, Mexico. *Geology*, 19, 867-871.

Howell, S. B. (2006). *Handbook of CCD astronomy (2nd ed.)*. Cambridge, UK: Cambridge University Press.

JPL (2019) *Small Body Database*. https://ssd.jpl.nasa.gov/sbdb.cgi

Kapteyn, J.C. (1905). Star Streaming. In J. Murray (Ed). *Seventy-fifth meeting of the British Association for the Advancement of Science* (pp.257-265). London, UK: Office of the Association.

Kepler, J. (1992). *New Astronomy*. (W.H. Donahue, Trans.). Cambridge, U.K., Cambridge University Press. (Original work published 1609).

Kron, K.C., Gordon, G.E. (1947). Photoelectric light-curves for RR Lyrae, Tu Cassipeiae, and T Monocerotis. *Publications of the Astronomical Society of the Pacific*, 59, 176.

Li, J-Y., Helfenstein, P., Buratti, B.J., & Takir, D. (2015). Asteroid Photometry. In Michel, P., DeMeo, F. E., & Bottke, W.F. (Eds.) *Asteroids IV* (pp. 129–150). Tucson, Az: The University of Arizona Press.

Lin, C., Ip, W., Lin, Z, Cheng, Y., & Lin, H. (2018) Photometric survey and taxonomic identifications of 92 near-Earth asteroids. *Planetary and Space Science*, 152, 116-135.

Loera-Gonzalez, P. Olguin, L., & Contreras, M.E., Morales, J.S., Schuster, W., & Sada, P.V. (2019). Results of the first semester of the 2018 Mexican asteroid photometry campaign. *Minor Planet Bulletin*, 46, 283-285.

Lowry, S.C., Fitzsimmons, A., Pravec, P., Vokrouhlicky, D., Boehnhardt, H., Taylor, P. A., Margo, J-L, Galad, A., Irwin, M., Irwin, J., & Kusnirak, P. (2007) Direct Detection of the Asteroidal YORP Effect. *Science*, 316, 272-274.

Lupishko, D.F., Kruglyi, Y.M, & Shevehenko, V.G. (2007). Photometry of Asteroids. *Kinematics and Physics of Celestial Bodies*, 23, 235-234.

Marsden, B.G. (1997). Overview of Orbits. *Annals of the New York Academy of Sciences*, 822,52-66.

Medeiros, H., Lazzaro, D. & Kodama, T. (2018) Spin distribution of asteroids – Statistical model revisited. *Planetary and Space Science*, 160, 77-83.

Menzel, R.L., & Roberge, W.G. (2013). Reexamination of the induction heating of primitive bodies in protoplanetary disks. *The Astrophysical Journal*, 776, 1-22.

Morbidelli, A., Bottke, W.F., Nesvorny D., & Levison, H.F. (2009). Asteroids were born big. *Icarus*, 204, 558-573.

Mohsen, A.M., Tompsett, M.F., & Sequin, C.M. (1975). Noise measurements in charge-coupled devices. *IEEE Transactions on Electron Devices*, 32, 209-218.

Nakamura, T., Noguchi, T., Tanaka, M., Zolensky, M.E., Kimura, M., Tsuchiyama, A., Nakato, A., Ogami, T., Ishida, H., Uesugi, M., Yada, T., Shirai, K., Fujimura, A., Okazaki, R., Sandford, S., Ishibashi, Y., Abe, M., Okada, T., Ueno, M., & Kawaguchi, J. (2011).

Itokawa dust particles: A direct link between S-Type asteroids and Ordinary Chondrites. *Science*, 333, 1113-1116.

O'Keefe, J.A. (1976). *Tektites and Their Origin: Developments in Petrology*. New York, Elsevier.

Opik, E.J. (1951) Collision probabilities with the planets and the distribution of interplanetary matter. *Proceedings of the Royal Irish Academy. Section A: Mathematical and Physical Sciences*, 54, 165-199.

Osip, D.J., Campins, H., & Schleicher, D. G. (1995) The rotation state of 4015 Wilson-Harrington: Revisiting origins for the near-Earth asteroids. *Icarus*, 114, 423-426.

Paddack, S.J. (1969). Rotational bursting of small celestial bodies: Effects of radiation pressure. *Journal of Geophysical Research*, 74, 4379-4381.

Park, R.S. (2019) *HORIZONS web-interface*. Solar System Dynamics. https://ssd.jpl.nasa.gov/horizons.cgi.

Pickering, E. C. (1882). The meridian photometer. *Monthly Notices of the Royal Astronomical Society*, 42, 365-367.

Pickering, E.C., Arthur, S., & Wendell, O.C. (1884). General catalogue. *Annals of Harvard College Observatory*, 14, 83-311.

Pickering, E.C. (1908a). Revised Harvard Photometry: A catalogue of the positions, photometric magnitudes and spectra of 9110 stars, mainly of the magnitude 6.50, and brighter observed with the 2 and 4 inch meridian photometers. *Annals of the Astronomical Observatory of Harvard College*, 50, 1-258.

Pickering, E.C. (1908b). A catalogue of 36,682 stars fainter than the magnitude 6.50 observed

with the 4-inch meridian photometer. *Annals of the Astronomical Observatory of Harvard College*, 54, 1-280.

Pogson, N. (1856). Magnitudes of Thirty-six of the Minor Planets for the first day of each month of the year 1857. *Monthly Notices of the Royal Astronomical Society*. 17: 12–15.

Polishook, D., Moskovitz, N., Binzel, R.P., Burt, B., DeMeo, F.E., Hinkle, M.L., Lockhart, M., Mommert, M., Person, M., Thirouin, A., Thomas, C.A., Trilling, D., Willman, M., & Aharonson, O. (2016). A 2 km-size asteroid challenging the rubble-pile spin barrier – A case for cohesion. *Icarus*, 267, 243-254.

Pravec, P., Harris, A.W. (2000) Fast and slow rotation of asteroids. *Icarus*, 148, 12-20.

Pravec, P., Harris, A.W., & Michalowski, T. (2002). Asteroid Rotations. In Bottke Jr., W.F., Cellino, A., Paolicchi, P., & Binzel, R.P. (Eds.) *Asteroids III*: (pp. 113–122). Tucson, Az: The University of Arizona Press.

Pravec, P., Kusnirak, P., Sarounova, L., Harris, A.W., Binzel, R.P., & Rivkin, A.S. (2002). Large Coherent Asteroid 2001 OE84. In Barbara Warmbein (ED.), *Proceedings of Asteroids, Comets, Meteors - ACM 2002. International Conference* (pp. 743 – 745). Noordwijk, Netherlands: ESA Publications Division.

Pravec, P., Scheirich, P., Kusnirak, P., Sarounova, L., Mottola, S., Hahn, G., Brown, P., Esquerdo, G., Kaiser, N., Krzeminski, Z., Pray, D.P., Warner, B.D., Harris, A.W., Nolan, M.C., Howell, E.S., Benner, L.A.M., Margo, J.-L, Galad, A., Holliday, W., … & Kober, G. (2006) Photometric survey of binary near-Earth asteroids. *Icarus*, 181, 63-93.

Ptolemy, C. (1984) *The Almagest*. (G.J. Toomer, Trans.). London, England: Gerald Duckworth & Co. Ltd. (Original work published circa 150 A.D.)

Radzievskii, V.V. (1952). A mechanism for the disintegration of asteroids and meteorites.

Astronomicheskii Zhurnal, 29, 162-170.

Reinhardt, J.C., Chen, x., Liu, W., Manchev, P., & Pate-Cornell, M.E. (2016). Asteroid risk assessment: A probabilistic approach. *Risk Analysis*, 26, 244-261.

Rozitis, B., Maclennan, E., & Emery, J.P. (2014). Cohesive forces prevent the rotational breakup of rubble-pile asteroid (29075) 1950 DA. *Nature*, 14, 174-184.

Rubincam, D.P. (2000). Radiative spin-up and spin-down of small asteroids. *Icarus*, 148, 2-11.

Safronov, V.S. (1972) *Evolution of the Protoplanetary Cloud and Formation of the Earth and the Planets (IPST Staff, Trans).* Jerusalem, Israel; Israel Program for Scientific Translation Ltd. (Original work published 1969)

Schulz, W.F. (1913). The use of the photo-electric cell in stellar photometry. *Astrophysical Journal*, 38, 187.

Schild, R. (1985). Early CCD observations of the halo of Halley's Comet. *Publications of the Astronomical Society of the Pacific*, 97, 1011-1012.

Shoemaker, E.M., Williams, J.C., Helin, E.F., & Wolfe, R.F. (1979) Earth-crossing asteroids: Orbital-classes, collision rates with Earth, and origin. In Gehrels, T. (Ed.) *Asteroids* (pp. 253-282), University of Arizona Press.

Smith, B.A. (1977). Uranus rings: an optical search. *Nature,* 268, 32.

Spoto, F., Tanga, P., Mignard, F., Berthier, J., Carry, B., Cellino, A., Dell'Oro, A., Hestroffer, D., Muinonen, K., Pauwels, T., Petit, J-M., David, P., De Angeli, F., Delbo, M., Frezouls, B., Galluccio, L., Granvik, M., Guiraud, J., Hernandez, J., … Zwitter, T. (2018). Gaia data release 2: Observations of solar system objects. *Astronomy & Astrophysics,* 616, A13.

Sonett, C.P., Colburn, D.S., Schwartz, K. (1968). Electrical heating of the meteorite parent

bodies and planets by dynamo induction from a pre-main sequence T Tauri "solar wind." *Nature*, 219, 924-926.

Stebbins, J. (1916). A study of β Lyrae with a photo-electric photometer; Photometric tests of θ Aquilae and σ Scorpii. *Lick Observatory Bulletin*, 277, 186-193.

Stetson, P.B., Vandenberg, D.A., Bolte, M., Hessers, J.E., & Smith, G.H. (1989). CCD photometry of the anomalous globular cluster Palomar 12. *The Astronomical Journal*, 97, 1360-1396.

Taylor, P.A., Margot, J-L., Vokrouhlicky, D., Scheeres, D.J., Pravec, P., Lowry, S.C., Fitzsimmons, A., Nolan, M.C., Ostro, S. J., Benner, L. A. M., Giorgini, J. D., & Magri, C. (2007) Spin rate of asteroid (54509) 2000 PH5 increasing due to the YORP Effect. *Science*, 316, 274-277.

Tholen, D.J. (1984) *Asteroid taxonomy from cluster analysis of photometry* (Doctoral dissertation). Retrieved from https://repository.arizona.edu/handle/10150/187738.

Thomas, C.A., Binzel, R.P. (2010). Identifying meteorite source regions through near-Earth object spectroscopy. *Icarus*, 205, 419-429.

Tricarico, P. (2016) The Near-Earth asteroid population from two decades of observations. *Icarus*, 284, 416-423.

Vernazza, P., Binzel, R.P., Thomas, C.A., DeMeo, F.E., Bus, S.J., Rivkin, A.S., & Tokunaga, A.T. (2008). Compositional differences between meteorites and near-Earth asteroids. *Nature*, 454, 858-860.

Veverka, J., Robins, M., Thomas, P., Murchie, S., Bell III, J.F., Izenberg, N., Chapman, C.,

Harch, A., Bell, M., Carcich, B., Cheng, A., Clark, B., Domingue, D., Dunham, D., Farquhar, R., Gaffey, M.J., Hawkins, E., Joseph, J., Kirk, R., Li, H., …&Yeomans, D.K. (2000). NEAR at Eros: Imaging and spectral results. *Science*, 289, 2088-2097.

Walsh, K.J., Richardson, D.C., & Michel, P. (2008) Rotational breakup as the origin of small binary asteroids. *Nature*, 454, 188-191.

Warner, B.D., Harris, A.W., & Pravec, P. (2009). The asteroid lightcurve database. *Icarus*, 202, 134-146.

Warner, B.D. (2011a). *The Asteroid Lightcurve Database*. http://www.minorplanet.info/lightcurvedatabase.html

Warner, B.D. (2011b). *MPO Canopus and PhotoRed reference guide*: Bdw Publishing.

Warner, B.D. (2012). *The MPO Users Guide*. Bdw Publishing.

Warner, B.D. (2016). *A practical guide to lightcurve photometry and analysis*. Switzerland: Springer International Publishing.

Warner, B.D. (2018) Near-Earth Asteroid lightcurve analysis at CS3-Palmer divide station: 2018 April-June. *The Minor Planet Bulletin*, 45, 366-379.

Warner, B.D., & Stephens, R.D. (2019). Near-Earth asteroid lightcurve analysis at the center for Solar System Studies: 2019 March-July. *Minor Planet Bulletin*, 46, 423-438.

Warner B.D., & Stephens, R.D. (2020). Near-Earth asteroid lightcurve analysis at the center for solar system studies: 2019 July-September. *Minor Planet Bulletin*, 47, 23-34.

Weidenschilling, S.J. (2010, March 1-5)). *Were asteroids born big? An alternative scenario* [Conference presentation]. 41st Lunar and Planetary Science Conference, Woodlands, TX, United States.

Willman, M., & Jedicke, R. (2011). Asteroid age distributions determined by space weathering

and collisional evolution models. *Icarus*, 211, 504-510.

Zacharias, N., Urban, S.E., Zacharias, M.I., Wycoff, G.L, Hall, D.M., Monet, D.G., & Rafferty, T.J. (2004). The second US Naval Observatory CCD Astrograph Catalog (UCAC2). *The Astronomical Journal*, 127, 3043-3059.

Zworykin, V.K., Morton, G.A., & Malter, L. (1936). The secondary emission multiplier – A new electronic device. *Proceedings of the Institute of Radio Engineers*, 24. 351-375.